



저작자표시-비영리-변경금지 2.0 대한민국

이용자는 아래의 조건을 따르는 경우에 한하여 자유롭게

- 이 저작물을 복제, 배포, 전송, 전시, 공연 및 방송할 수 있습니다.

다음과 같은 조건을 따라야 합니다:



저작자표시. 귀하는 원저작자를 표시하여야 합니다.



비영리. 귀하는 이 저작물을 영리 목적으로 이용할 수 없습니다.



변경금지. 귀하는 이 저작물을 개작, 변형 또는 가공할 수 없습니다.

- 귀하는, 이 저작물의 재이용이나 배포의 경우, 이 저작물에 적용된 이용허락조건을 명확하게 나타내어야 합니다.
- 저작권자로부터 별도의 허가를 받으면 이러한 조건들은 적용되지 않습니다.

저작권법에 따른 이용자의 권리는 위의 내용에 의하여 영향을 받지 않습니다.

이것은 [이용허락규약\(Legal Code\)](#)을 이해하기 쉽게 요약한 것입니다.

[Disclaimer](#)

Ph.D. DISSERTATION

A Si FET-type Gas Sensor with Pulse-driven
Localized Micro-heater for Low Power
Consumption

펄스 구동되는 저전력 로컬 마이크로 히터를 갖는
실리콘 FET형 가스 센서

BY

YOONKI HONG

August 2019

DEPARTMENT OF ELECTRICAL ENGINEERING AND
COMPUTER SCIENCE
COLLEGE OF ENGINEERING
SEOUL NATIONAL UNIVERSITY

A Si FET-type Gas Sensor with Pulse-driven Localized Micro-heater
for Low Power Consumption

펄스 구동되는 저전력 로컬 마이크로 히터를 갖는
실리콘 FET 형 가스 센서

지도교수 이 종 호

이 논문을 공학박사 학위논문으로 제출함

2019 년 8 월

서울대학교 대학원

전기컴퓨터공학부

홍 윤 기

홍윤기의 공학박사 학위논문을 인준함

2019 년 8 월

위 원 장 : 박 병 국 (인)

부위원장 : 이 종 호 (인)

위 원 : 황 철 성 (인)

위 원 : 장 호 원 (인)

위 원 : 권 혁 인 (인)

A Si FET-type Gas Sensor with Pulse-driven Localized
Micro-heater for Low Power Consumption

by

Yoonki Hong

Advisor: Jong-Ho Lee

A dissertation submitted in partial fulfillment of
the requirements for the degree of
Doctor of Philosophy
(Electrical Engineering and Computer Science)
in Seoul National University

August 2019

Doctoral Committee:

Professor Byung-Gook Park, Chair

Professor Jong-Ho Lee, Vice-Chair

Professor Cheol Seong Hwang

Associate Professor Ho Won Jang

Associate Professor Hyuck-In Kwon

ABSTRACT

Gas sensor technology plays a very important role in improving the quality of human life. Gas sensors are used not only to detect various harmful gases that cause air pollution and sick house syndrome, but also to diagnose diseases and to check the freshness of food materials. Four representative types of gas sensors are resistor-type, optical, electrochemical, and field effect transistor (FET)-type gas sensors. Among them, resistor-type gas sensor is the most studied type. Resistive sensors have a simple structure and are fabricated using a simple process, but they have a large sensing area in order to obtain a sufficient current level for operation. On the other hand, thanks to their CMOS compatibility, FET-type gas sensors can be fabricated in a very small size and can be integrated with CMOS integrated circuits (ICs) using the same fabrication process on the same wafer.

In this dissertation, a Si FET-type gas sensor with a horizontal floating-gate is fabricated by using conventional MOSFET fabrication process. The fabricated gas sensor features a micro-heater formed under the sensing part. Every gas reaction

between a target gas and a sensing material has its own optimal operating temperature. In order to control the operating temperature, gas sensors are equipped with micro-heaters in general. Since resistor-type sensors have a large sensing area, the size of micro-heater should also be large and thus they consume high power to heat the sensing layer. However, the fabricated gas sensor is designed to have a very small sensing area and a small-sized micro-heater so that the power consumption is low. The micro-heater is composed of heavily-doped poly-Si and is formed simultaneously with the poly-Si floating-gate without an additional photomask. An air gap is formed under the micro-heater in order to prevent the heat generated by the micro-heater from being dissipated. The air gap exists only in the vicinity of the sensing part, and is designed for the heat not to affect the FET of the sensor.

Furthermore, a method to read the temperature of micro-heater by measuring its resistance and a pulse operation scheme for gas-sensing are also proposed. Zinc oxide (ZnO) grown by atomic deposition method (ALD) is used as a sensing material and nitrogen dioxide (NO₂) and hydrogen sulfide (H₂S) are successfully detected at low power by using a pulse-driven micro-heater in the fabricated gas

sensor.

Keywords: Gas sensor, Si FET-type sensor platform, localized micro-heater,
pulse operation, temperature measurement method, low power.

Student number: 2013-20909

CONTENTS

Abstract.....	i
Contents.....	iv
List of Figures.....	viii
List of Tables.....	xvi

Chapter 1

Introduction.....	1
1.1. Various types of gas sensors.....	1
1.2. FET-type gas sensors.....	6
1.3. Micro-heaters embedded in gas sensors.....	12
1.4. Purpose of research.....	18
1.5. Dissertation outline.....	19

Chapter 2

Device structure and fabrication.....	20
2.1. Device structure.....	20
2.2. Device fabrication.....	22
2.2.1. Fabrication of Si FET-type sensor platform.....	22
2.2.2. Formation of air gap and sensing layer.....	24
2.3. Improvement in structural design of Si etching mask pattern.....	27
2.4. Characterization of ZnO sensing material.....	30
2.5. Current-voltage (I - V) characteristics.....	33

Chapter 3

Temperature measurement of poly-Si micro-heater.....	37
3.1. Electrical characterization of poly-Si micro-heater.....	37
3.1.1. Electrical resistivity of poly-Si.....	37
3.1.2. Contact resistance extraction.....	40
3.2. Resistance-temperature relation in poly-Si micro-heater.....	42

3.3. Measurement results.....	49
3.4. Temperature distribution in the fabricated gas sensor.....	58

Chapter 4

Gas-sensing characteristics.....	61
4.1. Sensing mechanism.....	61
4.1.1. Equivalent circuit of the fabricated gas sensor.....	61
4.1.2. H ₂ S-sensing mechanism.....	66
4.1.3. NO ₂ -sensing mechanism.....	68
4.2. Measurement setup.....	70
4.3. Measurement results.....	73
4.3.1. NO ₂ -sensing characteristics.....	73
4.3.2. H ₂ S-sensing characteristics.....	76
4.4. Pre-bias effect on sensing performance.....	79
4.5. Gas-sensing in stable NO ₂ ambience.....	83
4.6. Comparison in power consumption of micro-heaters.....	84

Chapter 5

Conclusion.....86

Bibliography.....88

Abstract in Korean.....99

List of Publications.....101

List of Figures

Fig. 1.1. Schematic setup of resistor-type gas sensor [13].	2
Fig. 1.2. Schematic drawing of optical gas-sensing measurement setup [16].	4
Fig. 1.3. Schematic diagram of an electrochemical ethylene (C ₂ H ₄) sensor [17].	5
Fig. 1.4. Schematic cross-sectional view of TFT gas sensor.	7
Fig. 1.5. Schematic cross-sectional view of catalytic metal gate FET sensor proposed by Lundström [23,38].	8
Fig. 1.6. Schematic cross-sectional views of (a) SGFET and (b) CCFET gas sensors [39].	9
Fig. 1.7. (a) SEM image and (b) schematic cross-sectional view of Si FET-type gas sensor [30].	11
Fig. 1.8. Pre-bias effects on (a) response and (b) recovery characteristics of Si FET-	

type gas sensor [32].11

Fig. 1.9. Schematic cross-sectional view of a conventional resistor-type gas sensor having a micro-heater.15

Fig. 2.1. (a) Top SEM image of the fabricated gas sensor having a localized poly-Si micro-heater. The brown and green shaded areas represent an air gap formed under the micro-heater and a ZnO sensing layer, respectively. (b) Schematic cross-sectional view cut along a yellow dotted line (A-A') in (a) [31].22

Fig. 2.2. Process flow of the Si FET-type gas sensor having a localized poly-Si micro-heater.25

Fig. 2.3. (a)-(g) Schematic bird's eye views of the key fabrication process steps.26

Fig. 2.4. (a) Optical microscopic image of the fabricated Si FET-type gas sensor platform with the initial design of Si etching mask pattern. (b) T_H - V_H curves of the sensor platform with the initial design as a parameter of Si etching time

(t_{etch}).29

Fig. 2.5. Comparison in T_H versus power consumption of micro-heater between the Si FET-type gas sensor platforms with the initial and modified designs.30

Fig. 2.6. XRD pattern of the ALD ZnO thin film deposited on a Si/SiO₂ substrate at 250°C.32

Fig. 2.7. (a) I_D - V_{CG} , (b) I_D - V_{DS} and (c) I_H - V_H curves of the fabricated Si FET-type gas sensor. The curves measured by DC and PIV methods are represented by lines and symbols, respectively. The PIV pulse scheme is depicted in the inset of (a) [31].35

Fig. 3.1. (a)-(d) Four poly-Si micro-heaters with different lengths used to obtain the resistivity of poly-Si. The length of a portion of each poly-Si micro-heater indicated by a yellow box is denoted as L_p38

Fig. 3.2. Resistance of micro-heater (R_H) versus length of a portion of micro-heater (L_p) (black line), and the linear fit of the R_H - L_p curve (red line). A DC bias of 1 V

was applied between the two electrodes to measure the currents.	40
Fig. 3.3. Approximation of the total length of the poly-Si micro-heater except the metal contact region (L_{poly}).	41
Fig. 3.4. Temperature (T) dependence of electrical conductivity (σ) for a doped semiconductor (n -type) [65]. n and μ represent carrier concentration and mobility of the semiconductor, respectively.	46
Fig. 3.5. Heavily n -type doped semiconductor [65]. A band overlapping the CB is formed by large number of impurities.	47
Fig. 3.6. (a) Change in T_{H} by raising the T_{plate} from 30 to 100°C (10°C step). No bias voltage is applied to the micro-heater. The T_{H} is measured by using infrared thermal microscopy [31]. (b) $R_{\text{H}}-T_{\text{plate}}$ as a parameter of V_{IT}	51
Fig. 3.7. Transient behaviors of (a) R_{H} and (b) T_{H} as a function of V_{H} [31], and (c) a measurement method for obtaining R_{H} after a 500 μs -long V_{H} pulse is applied at $t = 0$ s.	52

Fig. 3.8. Transient behaviors of (a) R_H and (b) T_H as a function of V_H [31], and (c) a measurement method for obtaining R_H after a 500 μs -long V_H pulse is turned off at $t = 0$ s.54

Fig. 3.9. $T_{H,\text{max}}$ versus frequency as a parameter of (a) V_H (50% of duty cycle) and (b) duty cycle ($V_H = 2$ V). The temperatures are obtained by using infrared thermal microscopy [31].57

Fig. 3.10. I_D - V_{CG} curves as a parameter of V_H (line) and T_{plate} (symbol) measured by DC method. The T_{HS} at V_{HS} of 0, 1, 1.5, 1.75 and 2 V are 25, 27, 50, 90 and 112°C, respectively [31].59

Fig. 3.11. (a) Optical microscopic image and (b) temperature distribution image of the gas sensor. The temperature distribution image is obtained by using thermoreflectance microscopy. The distance between the micro-heater and the channel is ~ 20 μm . A bias voltage of 2 V is applied to the micro-heater [31].60

Fig. 4.1. (a) Equivalent circuit of the Si FET-type gas sensor. (b) I - V characteristic

of the resistor-type gas sensor measured at 20°C and 180°C. The inset depicts a schematic cross-sectional view of the resistor-type sensor. (c) Simplified equivalent circuit [81].62

Fig. 4.2. Schematic energy band diagram of the gas sensor under flat band condition.

It was assumed that there are no charges in the oxide, nitrides, and interfaces.65

Fig. 4.3. Schematic energy band diagrams explaining the H₂S-sensing mechanism of the Si FET-type gas sensor.67

Fig. 4.4. H₂S-sensing characteristics of a Si FET-type gas sensor with a ZnO film as a sensing material [44]. (a) Negative V_{th} shift of I_D - V_{CG} curve. (b) Decrease of I_D68

Fig. 4.5. Schematic energy band diagrams explaining the NO₂-sensing mechanism of the Si FET-type gas sensor.69

Fig. 4.6. NO₂-sensing characteristics of a Si FET-type gas sensor with a ZnO film

as a sensing material [44]. (a) Positive V_{th} shift of I_D - V_{CG} curve. (b) Increase of I_D70

Fig. 4.7. Experimental setup for gas-sensing measurement. The three generated pulse signals are applied to the CG, the drain and the micro-heater [31].71

Fig. 4.8. Operation scheme of the fabricated gas sensor. V_{pre} and V_{rCG} are alternately applied to the CG. V_{rDS} is synchronized with V_{rCG} with a pulse width of t_{read} . V_H pulses are applied with a pulse width of t_H [31].72

Fig. 4.9. NO_2 -sensing measurement results. [31]. (a) Transient I_D behaviors to 500 ppb of NO_2 as a parameter of V_H . The t_H was 500 μs . (b) Transient I_D behaviors as a parameter of gas concentration. The V_H and the t_H were 2 V and 500 μs , respectively. (c) Sensor response versus NO_2 concentration as a parameter of V_H ($t_H = 500 \mu s$). (d) Transient I_D behaviors as a parameter of t_H ($V_H = 2 V$).74

Fig. 4.10. H_2S -sensing measurement results [31]. (a) Transient I_D behaviors to 10 ppm of H_2S as a parameter of V_H ($t_H = 500 \mu s$). (b) Transient I_D behaviors as a

parameter of gas concentration ($V_H = 2$ V, and $t_H = 500$ μ s). (c) Sensor response versus H₂S concentration as a parameter of V_H ($t_H = 500$ μ s). (d) Transient I_D behaviors as a parameter of t_H ($V_H = 2$ V).77

Fig. 4.11. Pre-bias effects on the detection of NO₂ and H₂S [31]. Transient responses to (a) 500 ppb of NO₂ and (b) 10 ppm of H₂S as a parameter of V_{pre} (-2 ~ 2 V). Solid and open symbols represent the transient I_D behaviors at a V_H of 2 and 0 V, respectively ($t_H = 500$ μ s, $V_{RCG} = V_{rDS} = -0.1$ V).82

Fig. 4.12. Sensor response ($|I_D|$) in stable NO₂ ambience as a function of $n \times t_H$. The NO₂ concentration and the t_H were 500 ppb and 500 μ s, respectively. The amplitude of the V_H pulse was 2 V ($V_{RCG} = V_{rDS} = -0.1$ V, and $V_{pre} = 0$ V).84

Fig. 4.13. Comparison in power consumption of the pulse-driven localized poly-Si micro-heater embedded in the Si FET-type gas sensor and the MEMS-based micro-heaters reported from the other groups.85

List of Tables

Table 1.1. Thermal conductivities of various materials.	16
Table 1.2. Recent studies on MEMS-based gas sensors with a micro-heater.	17
Table 3.1. L_{polySi} , R_{polySi} , and R_{cSi} of the four poly-Si micro-heaters having different lengths.	42

Chapter 1

Introduction

1.1. Various types of gas sensors

Gas-sensing technology gives great contributions to human life such as environmental monitoring, medical diagnosis, home and industrial safety, and so forth. Accordingly, various types of gas sensors have been studied and developed constantly. Among them, four representative types of gas sensors are introduced here: resistor-type [1-13], optical [14-16], electrochemical [17-19], and field-effect transistor-type (FET-type) gas sensors [20-32]. Resistor-type gas sensor is one of the most studied types of gas sensors. Target gases are detected by measuring the change in resistance of the device after the gas exposure as shown in Fig. 1.1 [13]. Resistor-type gas sensors are cheap and easy to fabricate. Thanks to the very simple structure of the resistor-type gas sensors, it is easy to apply various sensing materials to them such as semiconducting metal oxides [1-4], carbon nanomaterials (nanotubes [5,6], graphene-based materials [7,8]), transition metal dichalcogenides

(TMDs) [9,10], and so on. Moreover, many studies about the morphology [1,2] and chemical functionalization [3-5,10] of sensing materials based on resistor-type gas sensors could have been performed to enhance gas sensitivity. However, they should be large in size to reduce output variation and obtain enough working current. In addition, a large size of heater is required to raise the operating temperature due to its large sensing area, resulting in high power consumption [11,12,33].

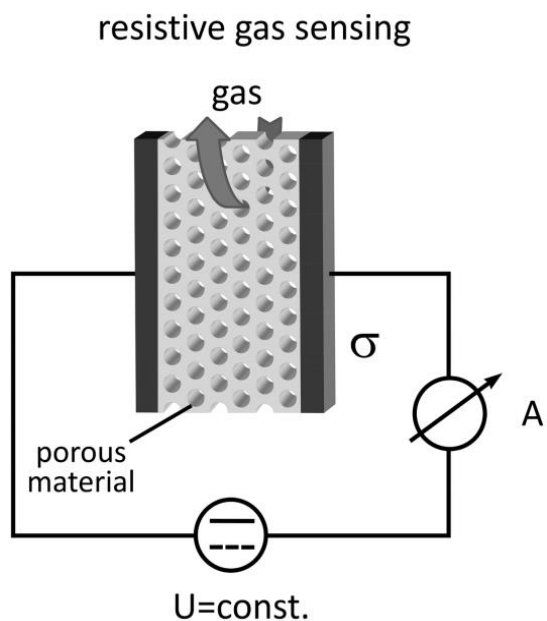


Fig. 1.1. Schematic setup of resistor-type gas sensor [13].

Optical gas sensors, in general, contain three major parts of light source, gas chamber, and light detector as depicted in Fig. 1.2 [16]. Every gas has its own absorbing property to light source at a specific wavelength. Thus, target gas molecules will absorb the radiation from the light source in its particular way and the presence of target gas can be detected and measured by the light detector [14,34]. Since the operating principle is only related to the physical property of target gas and does not accompany any chemical reaction between a target gas and this type of sensor, they offer high stability with little output drift and long lifetime. They also have high selectivity and fast response speed [15,34]. However, they are unsuitable for commercialization because they have demerits in miniaturization, low portability, and high cost. They are also affected due to ambient light interference [15,34,35].

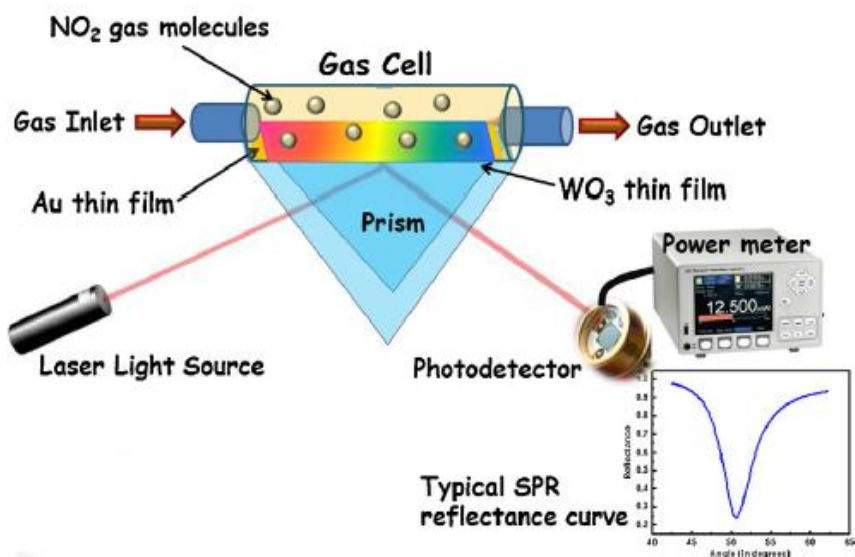


Fig. 1.2. Schematic drawing of optical gas-sensing measurement setup [16].

Electrochemical gas sensors consist of a working electrode, a counter electrode and an electrolyte solution in which the two electrodes are immersed as illustrated in Fig. 1.3 [17]. They sense target gases by measuring current or potential difference between the two electrodes generated by reduction or oxidation reaction on the working electrode [18,19,35]. They are sensitive to target gases at relatively low concentrations and possible to operate at low power. They are cheap and not easily affected by ambient vapors [21,35]. On the other hand, electrochemical sensors have a narrow operating temperature range since the electrolyte solution in this type

control the variation of output signals and calibrate the changes of the environmental conditions during sensing such as humidity, temperature and so on [36,37]. Therefore, thanks to easy integration with CMOS circuits in a single chip, FET-type gas sensors can attain a practical high accuracy gas-sensing system. Furthermore, they can be fabricated in very small size at low cost by using CMOS fabrication technology.

1.2. FET-type gas sensors

There are various types of FET-type gas sensors such as thin-film transistor (TFT) [20-22], catalytic metal gate FET [23-25], suspended gate FET (SGFET) [26,27], capacitively coupled FET (CCFET) [28,29] and Si FET having a horizontal floating-gate [30-32]. TFT gas sensor commonly has three terminals (gate, source and drain), utilizing a sensing material as its active layer (channel) as shown in Fig.

1.4. TFT gas sensors detect target gases by reading out the changed device parameters, resulting from charge transfer or redistribution in the active layer. They provide more parameters for measurement than resistor-type gas sensors, and thus

may give more detailed information about gas-sensing. Moreover, the detection limit and sensitivity are better than those of resistor-type sensors because of the signal amplification using a CMOS integrated circuit. However, like resistor-type gas sensors, TFT gas sensors need a large sensing area for stable output and consume high heater power.

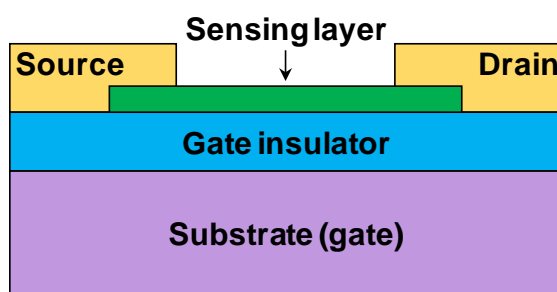


Fig. 1.4. Schematic cross-sectional view of TFT gas sensor.

Catalytic metal gate FET gas sensor was proposed for the first time by Lundström et al. in 1975 [23]. As displayed in Fig. 1.5, it has metal-insulator-semiconductor (MIS) structure and detects the change induced by dipole layer formed at the interface between the metal gate and the insulator by catalytic reaction of metal gate [23,38]. This sensor can be fabricated simply by using Si CMOS

technology and is compatible with CMOS circuits, but the size of target gas that can be detected is restricted because large-sized gas molecules are hard to penetrate through the metal gate. Also, there are limited kinds of metals that can be adopted for metal gates.

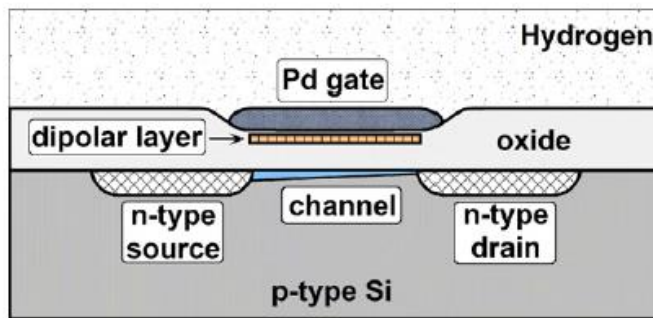


Fig. 1.5. Schematic cross-sectional view of catalytic metal gate FET sensor proposed by Lundström [23,38].

Fig. 1.6(a) and (b) show the schematic cross-sectional views of a SGFET and a CCFET gas sensors [39]. They both feature a suspended gate, which is covered with the sensing layer, and an air gap formed between the sensing layer and an FET. Target gases can flow through the air gap and the sensing layer generates a potential

difference during sensing. SGFETs and CCFETs can overcome the limitations of catalytic metal gate FET gas sensors. The air gap enables them to detect any size of gas molecules. As the flip chip mounting technology is applied for forming the sensing layer, a desired sensitive layer can be applied. Due to the presence of air gap, however, these types of sensors have low sensitivity and a poor gate coupling. The fabrication process is difficult and complicated because it requires at least eight photomasks and the flip chip process.

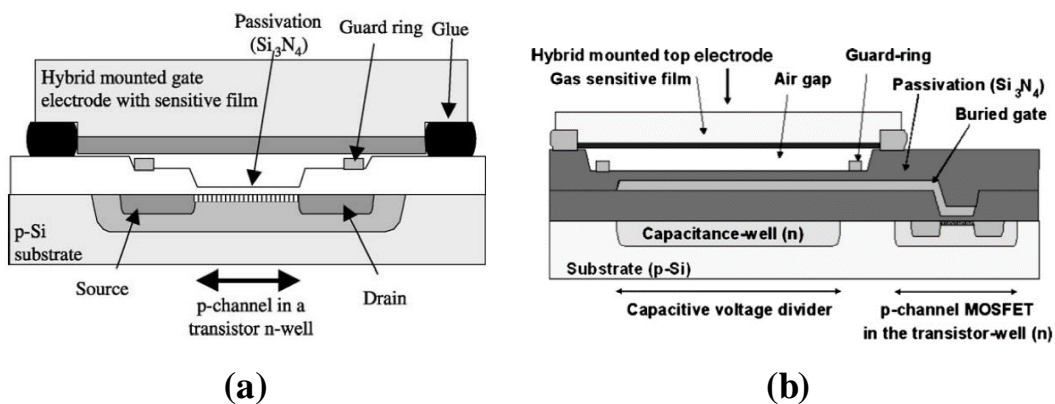


Fig. 1.6. Schematic cross-sectional views of (a) SGFET and (b) CCFET gas sensors [39].

To remedy the shortcomings of SGFET and CCFET gas sensors, Si FET-type gas sensor having a horizontal floating-gate was first proposed by our group [30]. In this dissertation, this type of sensor is called Si-FET type gas sensor. As shown in Fig. 1.7(a) and (b), the sensor has a control-gate (CG) and a floating-gate (FG) facing each other and a sensing layer is formed between them. Thus, a high gate coupling can be achieved if the two electrodes face each other in an interdigitated form, and the fabrication process is simpler than that of SGFET or CCFET. In order to improve the sensing characteristics of Si FET-type gas sensors, a pre-bias pulse measurement method was proposed [32]. Appropriate pre-biases and read biases are applied alternatively to the CG during the measurement. The polarity and magnitude of the pre-bias will affect both the response and the recovery characteristics, as shown in Fig. 1.8(a) and (b), so that the sensing performance was effectively enhanced without introducing any extra bulky equipment (light source and etc.). In addition, as the read operation is limited within few decades of microseconds, the possibility of charge trapping inside the sensors was dramatically restrained.

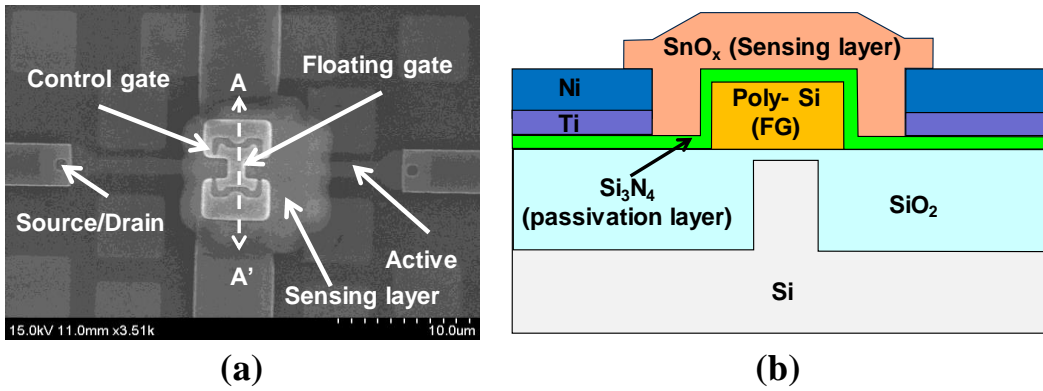


Fig. 1.7. (a) SEM image and (b) schematic cross-sectional view of Si FET-type gas sensor [30].

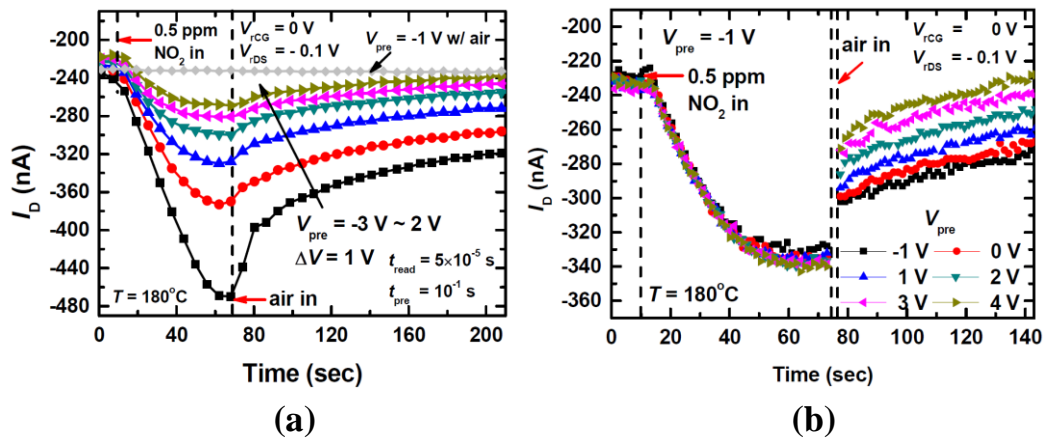


Fig. 1.8. Pre-bias effects on (a) response and (b) recovery characteristics of Si FET-type gas sensor [32].

1.3. Micro-heaters embedded in gas sensors

Recently, studies on gas-sensing at room temperature (RT) are increasing [40-43]. Gas-sensing at RT does not require a micro-heater in the sensor and thus the power consumption can be reduced. To realize gas detection at RT, sensing materials are structurally or morphologically modified [40,41] or decorated with metal nanoparticles as a catalyst [42,43] during the device fabrication. However, these sensors have low reliability and the fabrication yield is low due to very complicated and difficult fabrication process. Most of the gas sensors having metal oxides as a sensing material still operate at high temperature. Every gas reaction between a target gas and a sensing material has its own optimal operating temperature. In other words, an optimal operating temperature depends on target gas or sensing material. In [44], a zinc oxide (ZnO) thin film as a sensing material was adopted for a Si FET-type gas sensor to detect seven different target gases: nitrogen dioxide (NO₂), hydrogen sulfide (H₂S), ammonia (NH₃), sulfur dioxide (SO₂), carbon dioxide (CO₂), methane (CH₄), propane (C₃H₈). Unlike the other five target gases showing the negligible sensor responses, NO₂ and H₂S were found to

be detectable but the optimal operating temperatures are different (180°C for NO₂ and 150°C for H₂S). In [45], the sensing characteristics of the resistor-type hydrogen (H₂) sensors were investigated. A pure ZnO sensing material showed its maximum response at the optimal operating temperature of 400°C whereas all the RGO/ZnO composites exhibited their maximum responses at the optimal operating temperature of 150°C. Meanwhile, the optimal operating temperature of the resistor-type H₂ sensor having a tin dioxide (SnO₂) sensing material was 265°C in [46]. For metal oxide-based gas sensors, it is well-known that reducing gases such as H₂S, NH₃ and carbon monoxide (CO) react with oxygen ions adsorbed on the surface of metal oxides, resulting in the electron transfer from the oxygen ions to the metal oxides. It is also known that metal oxide-based sensors have the optimal operating temperatures of 200-400°C [47], at which oxygen molecules in air are easily adsorbed at the surface of the metal oxides by trapping electrons from the conduction band (CB) of the metal oxides [47]. Therefore, a higher sensor response can be achieved by raising an operating temperature close to the optimal operating temperature. To raise the operating temperature, hot chuck or micro-heater has been

used in general.

Raising the operating temperature also reduces response and recovery times of sensors. It is due to the fact that the kinetic energy of target gas molecules increases with increasing operating temperature, resulting in the increase of reaction rate with a sensing material. In the NO₂-sensing measurements in [44], response time reduces and recovery rate increases as operating temperature rises.

Fig. 1.9 shows a schematic cross-sectional view of a conventional resistor-type gas sensor having a micro-heater. This type of sensor is fabricated by using microelectrochemical systems (MEMS) fabrication technology. Compared to complementary metal-oxide-semiconductor (CMOS) technology, MEMS fabrication process is less complicated and involves more variety of materials. However, it has disadvantage in size and compatibility with integrated circuits (ICs). The key fabrication process of the resistor-type sensor will be explained briefly as follows. An insulation layer is formed on a substrate and a heating element as a micro-heater is patterned. In typical, platinum (Pt), tungsten (W) and gold (Au) are representative metals used as a micro-heater. Heavily-doped poly-Si has also been

widely used. After forming the micro-heater, an insulation layer and a passivation layer are sequentially covered on the micro-heater. Electrodes, which has an interdigitated shape in general, are then formed and a sensing material is deposited to fill a gap between the electrodes. Finally, the backside of the substrate is etched to form a cavity which prevents the heat dissipation. This is because air has a very low thermal conductivity compared to other materials as displayed in Table 1.1.

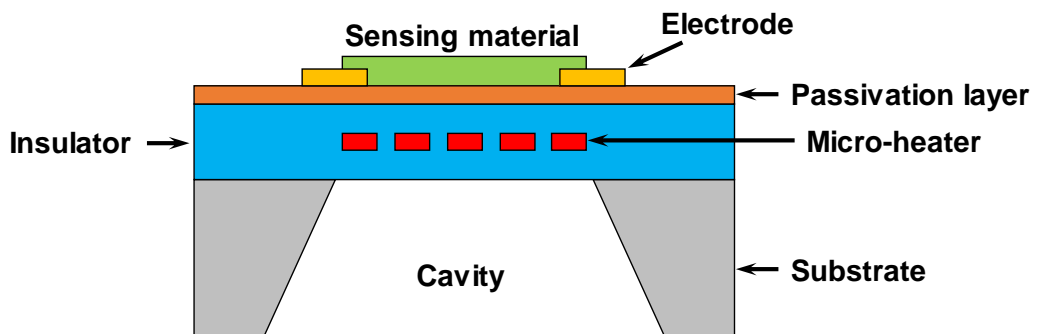


Fig. 1.9. Schematic cross-sectional view of a conventional resistor-type gas sensor having a micro-heater.

Table 1.1. Thermal conductivities of various materials

	Thermal conductivity (W/m·K)
Air	0.024
Si	130
SiO₂	1.4
Si₃N₄	9-30
Poly-Si	30-40
Cr	93.7
Au	317

Table 1.2 shows a summary of the recent studies on MEMS-based gas sensors with a micro-heater reported by other research groups [11,12,33]. The sizes of all the micro-heaters shown in Table 1.2 are large so that they consume high power. In this study, however, a Si FET-type gas sensor has a small-sized sensing area thanks to its compatibility with CMOS technology and thus it has a very small poly-Si micro-heater [31]. Therefore, the power consumption of micro-heater can be reduced. Moreover, in order to further diminish the power consumption, a pulse scheme for simultaneous operation of the FET and the micro-heater of the sensor is proposed.

Table 1.2. Recent studies on MEMS-based gas sensors with a micro-heater.

Sensor type	Sensing material	Micro-heater	Size	Power	Ref.
Resistor	Pd/SnO ₂	Pt	0.4 × 0.4 mm ²	45 mW @ 300°C	[11]
Resistor	SnO ₂	Poly-Si	50 × 50 μm ²	7 mW @ 200°C	[12]
MEMS-based FET	Graphene/Pd-Ag	Pt	0.1 × 1.2 mm ²	45.4 mW @ 150°C	[33]

1.4. Purpose of research

Sensor response to a target gas increases by raising the temperature to the optimal operating temperature at which the sensor response is maximized. Also, response and recovery times are reduced by raising the operating temperature. In order to control the operating temperature, gas sensors are equipped with a micro-heater. For resistor-type gas sensors, the size of sensing area is so large that the size of micro-heater should be large to heat the sensing layer. As a result, the power consumed by the micro-heater is very high.

In this dissertation, a Si FET-type gas sensor having a localized poly-Si micro-heater is proposed to reduce heater size and power consumption. It has an air gap under the heater to prevent the heat dissipation. It is verified that the micro-heater temperature can be read by reading the micro-heater resistance. The micro-heater temperature driven by a series of pulse-type heating bias is identified by the proposed method and the infrared thermal microscopy. The NO₂ and H₂S sensing characteristics are investigated by applying a pulse operation scheme to the FET and the micro-heater of the fabricated gas sensor.

1.5. Dissertation outline

This dissertation is organized as follows. Chapter 1 contains an overview of gas sensor technology by introducing various types of gas sensors. Then, the advantages of FET-type gas sensors are presented compared with other types of gas sensors. After that, the purpose of using micro-heaters in gas-sensing is described and the research reports on resistor-type or MEMS-based FET-type gas sensors with a micro-heater are investigated. The purpose of research and the outline of dissertation are also presented. In Chapter 2, the structure and the fabrication process of a Si FET-type gas sensor having a localized poly-Si micro-heater are explained in detail. Then, the ZnO sensing material, the FET, and the micro-heater are characterized. In Chapter 3, a method for reading the temperature of micro-heater is proposed. Then, the temperature driven by a series of pulse-type heating bias is identified by infrared thermal microscopy and thermorefectance microscopy. Chapter 4 includes the explanation on sensing mechanism and the discussion on the results of the gas-sensing measurements obtained by applying a proposed pulse operation scheme. Finally, the conclusion is presented in Chapter 5.

Chapter 2

Device structure and fabrication

2.1. Device structure

Fig. 2.1(a) shows a top scanning electron microscopic (SEM) image of the fabricated FET-type gas sensor having a localized poly-Si micro-heater. A control-gate (CG) and a floating-gate (FG) are formed horizontally in an interdigitated shape to increase the coupling ratio between them. A gap between the CG and the FG is about $0.5\ \mu\text{m}$. An *n*-type semiconducting zinc oxide (ZnO) used as a sensing layer covers the part of the CG and the FG, and also fills the gap between them. A poly-Si micro-heater is designed to heat only the sensing part and its size is $\sim 15 \times 5\ \mu\text{m}^2$. The width and the thickness of the micro-heater are $2\ \mu\text{m}$ and $350\ \text{nm}$, respectively. To prevent the heat dissipation generated by the micro-heater, an air gap is formed at a depth of $\sim 10\ \mu\text{m}$ under and around the sensing part. However, it does not reach the FET of the sensor in order not to damage it. The bridges are designed between the etching patterns for forming the air gap along the micro-

heater in order to sustain the sensing part structurally. The width of the bridge is 0.5 μm . The width/length of the channel is 2 μm / 2 μm . Fig. 2.1(b) shows a schematic cross-sectional view of the gas sensor cut along a yellow dotted line A-A' in Fig. 2.1(a). The FG and the micro-heater which are composed of heavily *n*-doped poly-Si are simultaneously formed on the field oxide and the gate oxide, respectively. This reduces the number of photomasks used for the fabrication by one compared to using a micro-heater composed of metal. The CG and the micro-heater are electrically insulated by a SiO₂ (10 nm)/Si₃N₄ (20 nm)/SiO₂ (10 nm) (ONO) layer. Since the sensing layer and the micro-heater are spaced apart by only the thickness of the ONO layer, the heat generated by the micro-heater is effectively transferred to the sensing layer. The sensing layer is also insulated by the ONO layer from the FG while it is connected to the CG. Thus, the sensing layer is considered to act as a gate of the sensor. The Si₃N₄ in the ONO layer serves as a passivation layer to prevent the sensing material from contaminating the FET [48].

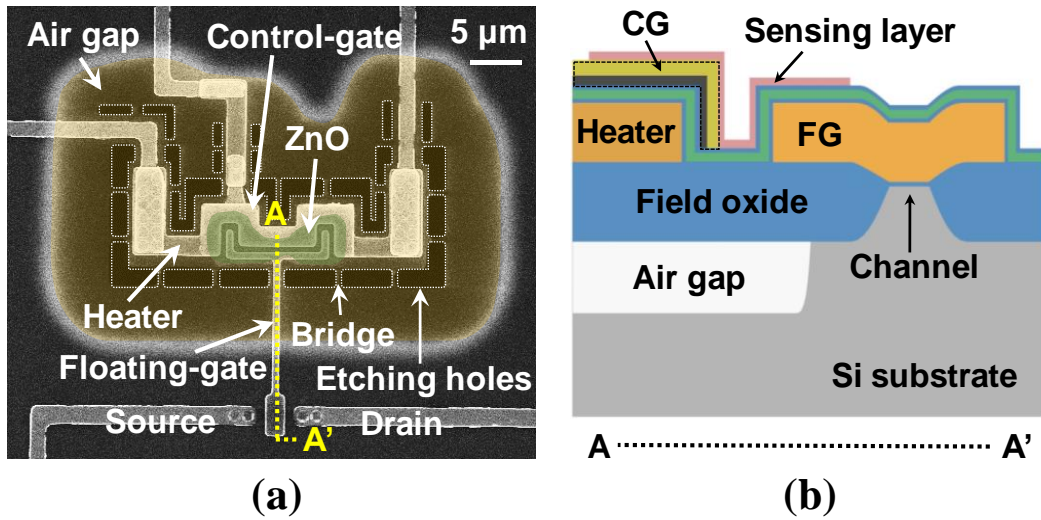


Fig. 2.1. (a) Top SEM image of the fabricated gas sensor having a localized poly-Si micro-heater. The brown and green shaded areas represent an air gap formed under the micro-heater and a ZnO sensing layer, respectively. (b) Schematic cross-sectional view cut along a yellow dotted line (A-A') in (a) [31].

2.2. Device fabrication

2.2.1. Fabrication of Si FET-type sensor platform

A Si FET-type gas sensor having a localized poly-Si micro-heater is fabricated on a 6-inch Si wafer by using six photomasks and Si FET technology. The gas sensor is based on *p*MOSFET because it has less flicker noise than *n*MOSFET [49].

Figs. 2.2 and 2.3 show the process flow of the Si FET-type gas sensor having a localized poly-Si micro-heater and the schematic bird's eye views of the key fabrication process steps, respectively. An *n*-type Si (100) wafer was cleaned by using the standard wafer cleaning procedure which consists of a RCA chemical cleaning followed by a dipping in a hydrofluoric acid (HF) solution to remove a native oxide. A 10 nm-thick SiO₂ layer was thermally grown and a 150 nm-thick Si₃N₄ layer was then deposited on the Si wafer by low pressure chemical vapor deposition (LPCVD). A photomask was formed on the Si₃N₄ layer by photolithography (SS03A9, 1st) and the Si₃N₄ and the SiO₂ layer were sequentially dry-etched for defining the active region of the FET. Then, a 550 nm-thick SiO₂ layer as a field oxide was thermally grown to electrically isolate the active region by using local oxidation of silicon (LOCOS) technique. After removing the Si₃N₄ and the SiO₂ layer, the buried-channel implantation was performed for reducing flicker noise. A layer of 10 nm-thick SiO₂ was thermally grown as a gate oxide on the active region and a 350 nm-thick *in situ* *n*⁺-doped poly-Si was deposited and patterned by using a photomask (SS03A9, 2nd) to form a FG and a micro-heater.

After the S/D implantation, an ONO layer was formed: Thermal oxidation followed by the sequential deposition of Si_3N_4 and SiO_2 by LPCVD. Then, a photomask was patterned (SS03A9, 3rd) and the ONO layer was dry-etched to define the metal contact holes. After that, a photomask was patterned to form the electrodes for the CG, source, drain, and micro-heater (AZ5214, 4th). Cr (30 nm) and Au (50 nm) were deposited by sputtering method, and patterned by lift-off method.

2.2.2. Formation of air gap and sensing layer

To form an air gap under the micro-heater, a photomask was patterned (SS03A9, 5th) and the field oxide along the edge of the micro-heater was etched by an inductively coupled plasma (ICP) etching process using CF_4 gas. It has been reported that SiO_2 film is anisotropically etched in CF_4/O_2 condition [50]. Then, a deep reactive ion etching (DRIE) process with SF_6/Ar gas was performed for isotropic etching of Si substrate to form the air gap [51]. Finally, a ZnO film as a sensing material was formed by using atomic layer deposition (ALD) method. A 15 nm-thick of the ZnO film was deposited on the wafer and a photomask was

patterned to conceal only the sensing part (AZ5214, 6th). Then, the wafer was dipped in a HF solution to etch the unwanted part of the ZnO film and the photomask was removed.

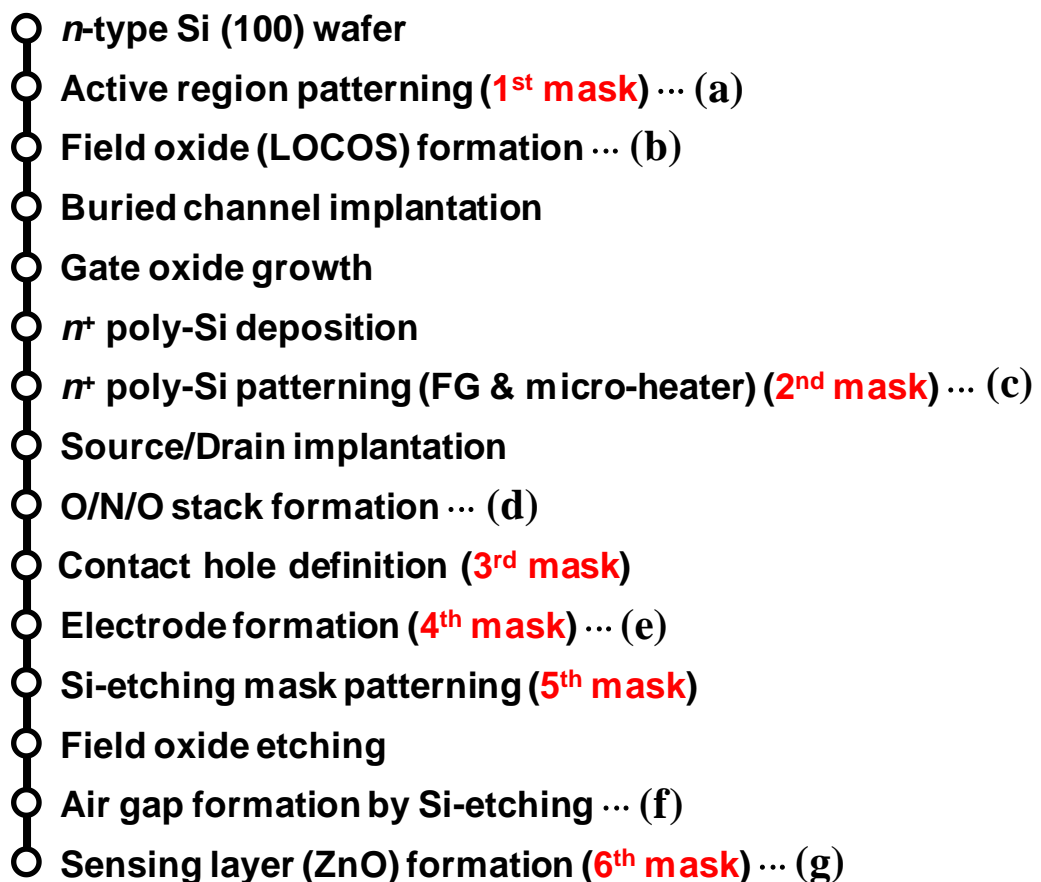


Fig. 2.2. Process flow of the Si FET-type gas sensor having a localized poly-Si micro-heater.

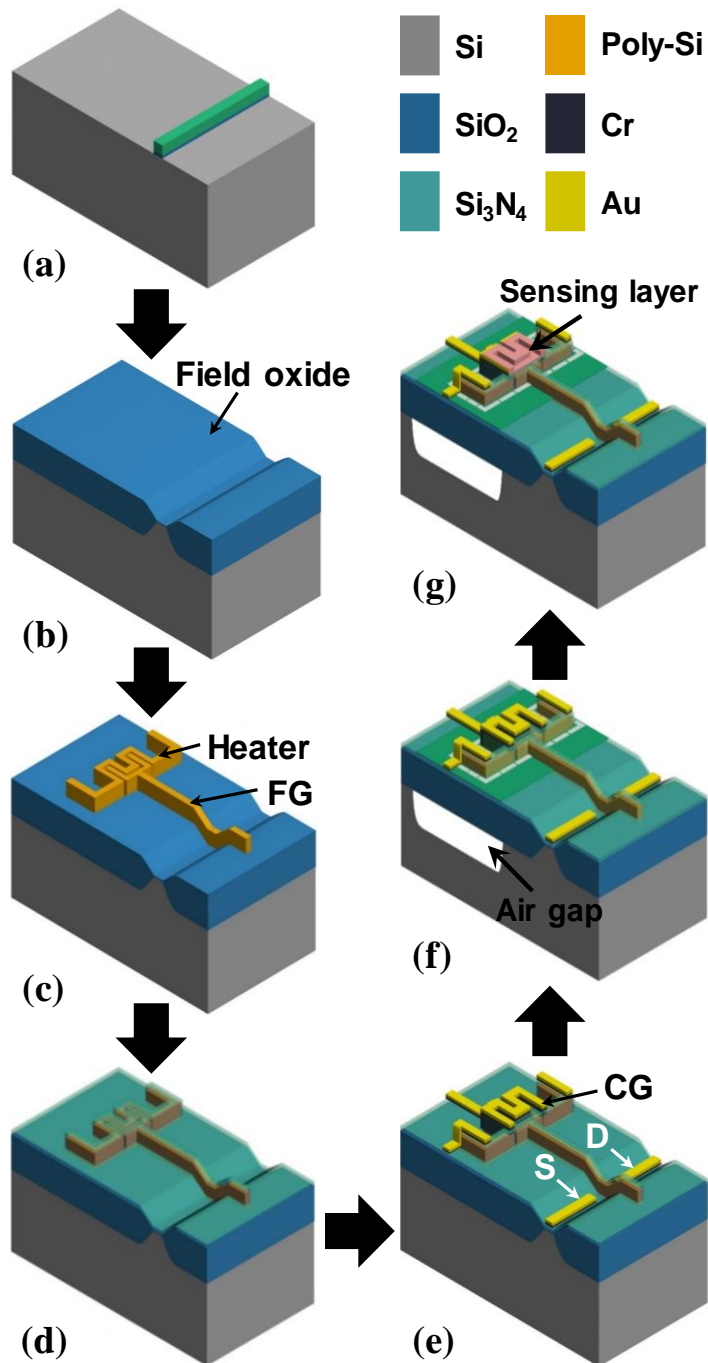
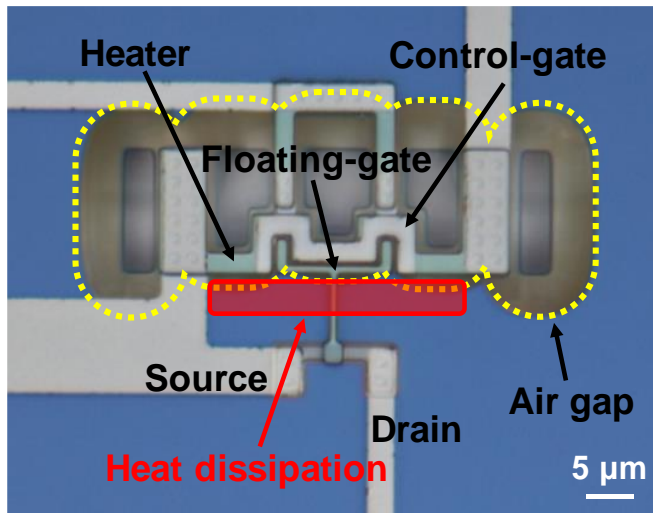


Fig. 2.3. (a)-(g) Schematic bird's eye views of the key fabrication process steps.

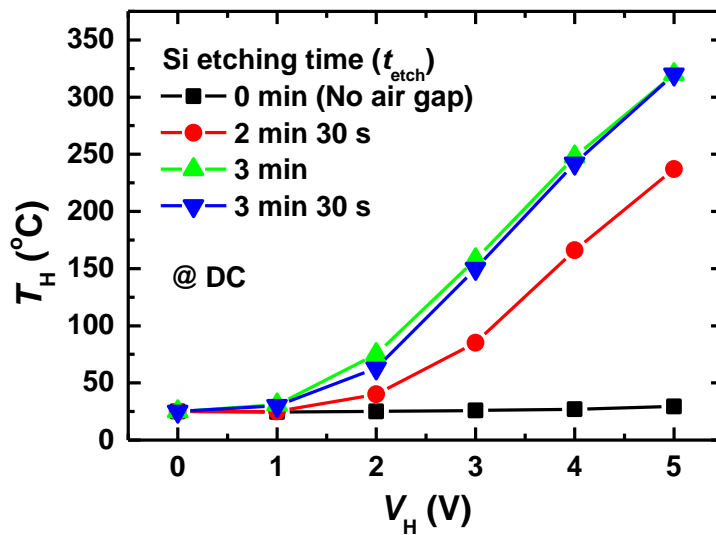
2.3. Improvement in structural design of Si etching mask pattern

The structural design of Si etching mask pattern for forming an air gap under and around the micro-heater in the Si FET-type gas sensor has been improved to minimize the heat dissipation. Fig. 2.4(a) depicts the initial design of Si etching mask pattern applied to the fabricated Si FET-type gas sensor platform. A yellow dotted line indicates an area where the air gap under the micro-heater is formed. Fig. 2.4(b) shows the T_H - V_H curves of the micro-heater as a function of Si etching time (t_{etch}). The T_{HS} were obtained by using infrared thermal microscopy. In Fig. 2.4(b), as t_{etch} increases, the heat dissipation decreases due to the increase in size of the air gap, and thus T_H rises at a certain V_H . However, if $t_{\text{etch}} > 3$ min, T_H no more increases since Si etching rate is saturated. In the initial design, the air gap does not seem to be formed between the micro-heater and the channel of the FET as represented by a red shaded rectangle in Fig. 2.4(a). It was assumed that this would cause the heat dissipation of the micro-heater. Therefore, the design has been modified to have the extra etching mask patterns between the micro-heater and the channel, and along

the metal lines connected to the electrodes for the CG and the micro-heaters, as displayed in Fig. 2.1(a). The V_{HS} versus micro-heater power of the micro-heaters with the initial and the modified designs of the etching mask patterns were obtained as shown in Fig. 2.5. If the same micro-heater power is consumed, the T_H with the modified design is higher than that with the initial design. From this result, it was demonstrated that the design modification helps to reduce the heat dissipation of the micro-heater.



(a)



(b)

Fig. 2.4. (a) Optical microscopic image of the fabricated Si FET-type gas sensor platform with the initial design of Si etching mask pattern. (b) T_H - V_H curves of the sensor platform with the initial design as a parameter of Si etching time (t_{etch}).

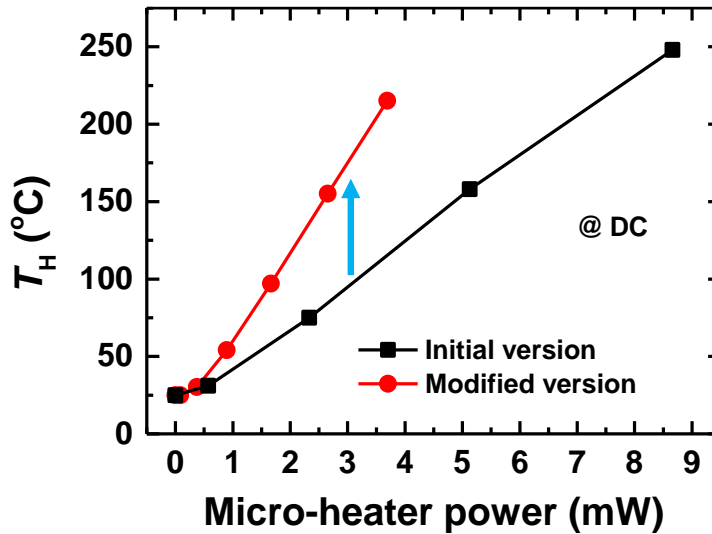


Fig. 2.5. Comparison in T_H versus power consumption of micro-heater between the Si FET-type gas sensor platforms with the initial and modified designs.

2.4. Characterization of ZnO sensing material

The X-ray diffraction (XRD) measurement was performed for the structural analysis of the ZnO sensing material. A sample of a 15 nm-thick ALD ZnO film for the XRD measurement was prepared on a Si/SiO₂ substrate by using the same deposition condition as was used for the fabricated gas sensor. Fig. 2.6 displays the XRD pattern of the ZnO film. The diffraction peaks corresponding to the reflection from (002), (102) and (103) were observed in the ZnO film, which represents that

the ZnO film has polycrystalline wurtzite structure [52,53].

The electrical parameters of the ZnO film, such as the carrier concentration (N_d), resistivity (ρ) and mobility (μ), can be found in [54]. In this work, the ALD ZnO film was deposited at 250°C by using diethylzinc ($Zn(C_2H_5)_2$, DEZ) as a precursor and ozone (O_3) as an oxidant, which was also adopted for the ZnO film in [54] by using the same equipment as was used in this work. The N_d , ρ and μ are considered to be $3 \times 10^{18} \text{ cm}^{-3}$, $2 \text{ } \Omega \cdot \text{cm}$ and $2 \text{ cm}^2/\text{V} \cdot \text{s}$, respectively.

By using the N_d obtained above, the Debye length of the ZnO film (L_D) can also be calculated as below:

$$L_D = \sqrt{\frac{\varepsilon k_B T}{q^2 N_d}} \quad (1)$$

where ε and k_B are the permittivity of the ZnO film and the Boltzmann's constant, respectively [55]. Taking the ε from [52], where the static dielectric constant of ALD ZnO deposited at 250°C is 18.34, the L_D of the ZnO film at 25°C is 2.97 nm.

The Debye length, which is defined and valid for a point charge, is commonly used

to estimate the width of the depletion layer induced by the gas reaction. However, in this study, the change in sheet charge density is caused mostly at the interface between the ZnO layer and the ONO layer by the gas reaction, which changes the depletion width. Therefore, the depletion width is expected to be more accurate than the Debye length.

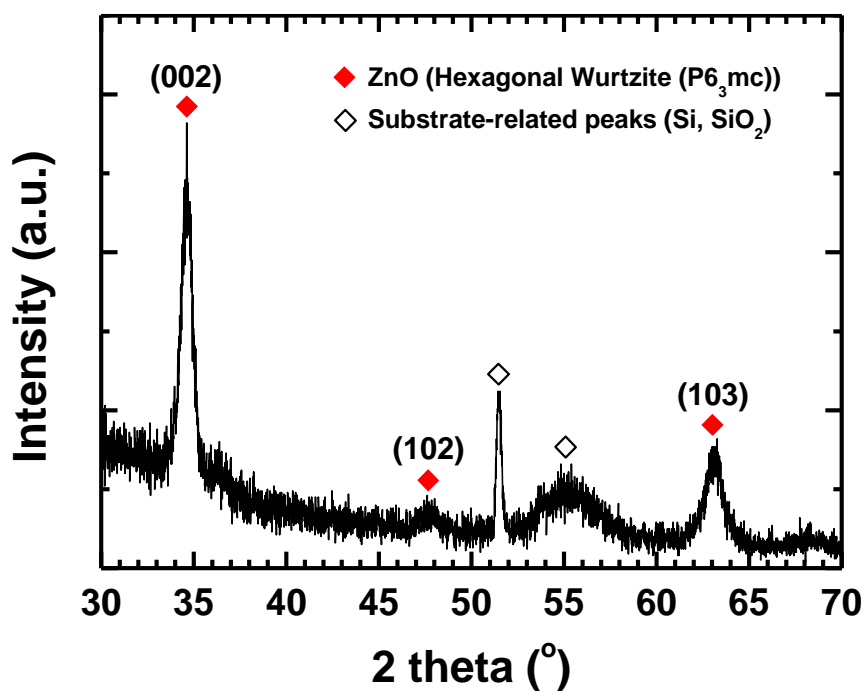


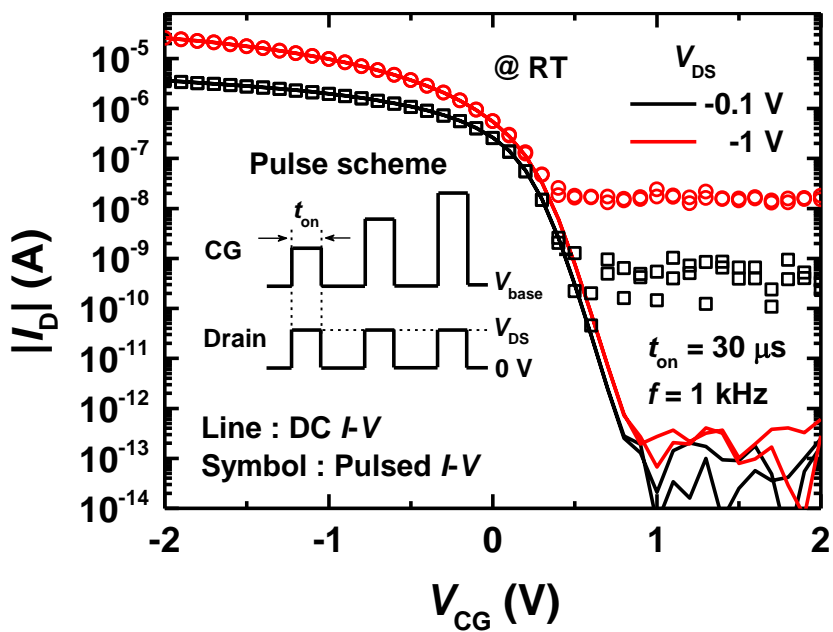
Fig. 2.6. XRD pattern of the ALD ZnO thin film deposited on a Si/SiO₂ substrate at 250°C.

2.5. Current-voltage (I - V) characteristics

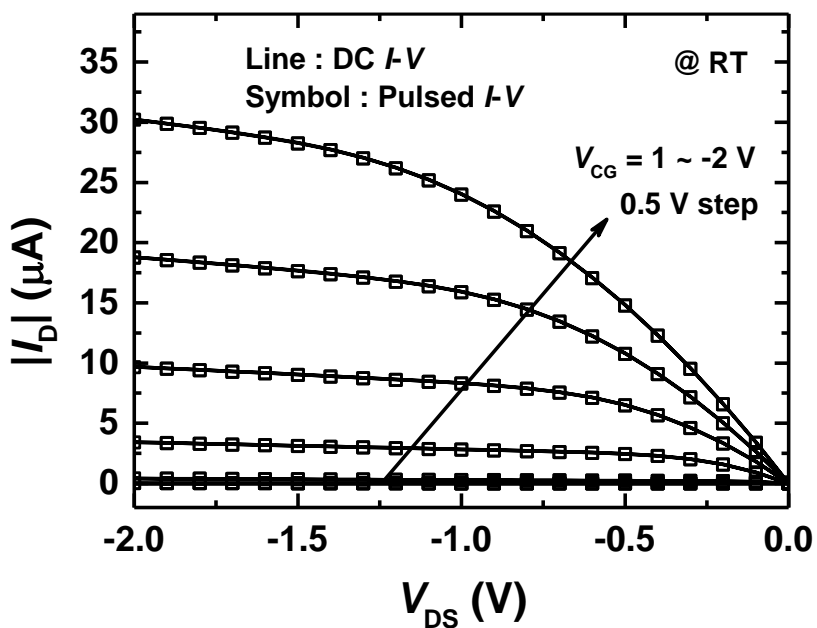
The transfer (I_D - V_{CG}) and the output (I_D - V_{DS}) characteristics of the fabricated gas sensor were measured at 25 °C by using direct current (DC) and pulsed I - V (PIV) methods. Current of the micro-heater (I_H) versus heating bias (V_H) was also measured by DC and PIV methods. The PIV method was used to minimize the electrical stress on the device which results in current drifting in measurements due to trapped charge. A semiconductor parameter analyzer (B1500A, Keysight Technologies), which was equipped with four Semiconductor Measurement Units (SMU) and two Waveform Generator Fast Measurement Units (WGFMU, B1530A, Keysight Technologies), and a probe station were used for measuring the electrical properties of the gas sensor.

Fig. 2.7(a) shows the I_D - V_{CG} curves of the gas sensor at drain-to-source biases (V_{DS}) of -0.1 and 1 V obtained by DC (line) and PIV (symbols) measurements. The pulse scheme used for the PIV measurements are shown in the inset of Fig. 2.7(a). The two synchronized pulses are individually applied to the CG and the drain with a pulse width (t_{on}) of 30 μ s at a frequency of 1 kHz (with the source grounded). The

base voltage for the pulses is 0 V. The high off-current level measured by the PIV method in Fig. 2.7(a) results from the measurement system noise [56]. Fig. 2.7(b) represents the I_D - V_{DS} curves of the gas sensor at control-gate biases (V_{CG}) ranging from 1 to -2 V. As in Fig. 2.7(a), the two synchronized pulses with a t_{on} of 30 μ s at 1 kHz are used. Fig. 2.7(c) shows the I_H - V_H curves of the micro-heater. Unlike the curve measured by the PIV method ($t_{on} = 30 \mu$ s at 1 kHz), the DC I_H - V_H curve is nonlinear due to the increase of micro-heater resistance (R_H) resulting from Joule heating. The detailed explanation on the relation between R_H and micro-heater temperature (T_H) in Section 3.2.



(a)



(b)

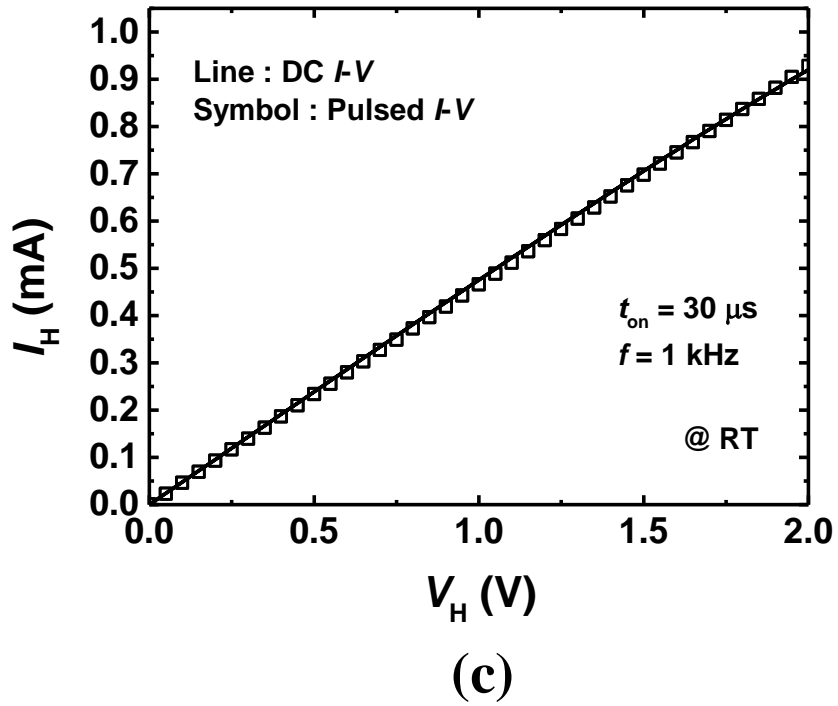


Fig. 2.7. (a) I_D - V_{CG} , (b) I_D - V_{DS} and (c) I_H - V_H curves of the fabricated Si FET-type gas sensor. The curves measured by DC and PIV methods are represented by lines and symbols, respectively. The PIV pulse scheme is depicted in the inset of (a) [31].

Chapter 3

Temperature measurement of poly-Si micro-heater

3.1. Electrical characterization of poly-Si micro-heater

3.1.1. Electrical resistivity of poly-Si

The resistivity of poly-Si is an essential parameter for extracting the contact resistance between poly-Si micro-heater and contact electrode. The contact resistance is closely related to the performance of the micro-heater. As contact resistance increases, the heat generated by contact resistance increases whereas the heat generated by the micro-heater located under the sensing part is relatively reduced, resulting in the increase in heat dissipation. Also, as the heat generated by the contact resistance increases, the contact is liable to be damaged by the heat.

To obtain the resistivity of poly-Si, the four micro-heaters with different lengths were used as a pattern for transmission line measurement (TLM) method,

which is most commonly used to extract the specific contact resistance [57,58].

Only the lengths of a portion of the poly-Si micro-heaters (L_p), indicated by yellow rectangles as shown in Fig. 3.1(a)-(d), are different but the dimensions of the other portions are all the same. Note that the dimensions of the metal pads, metal lines and metal contact areas are also all the same.

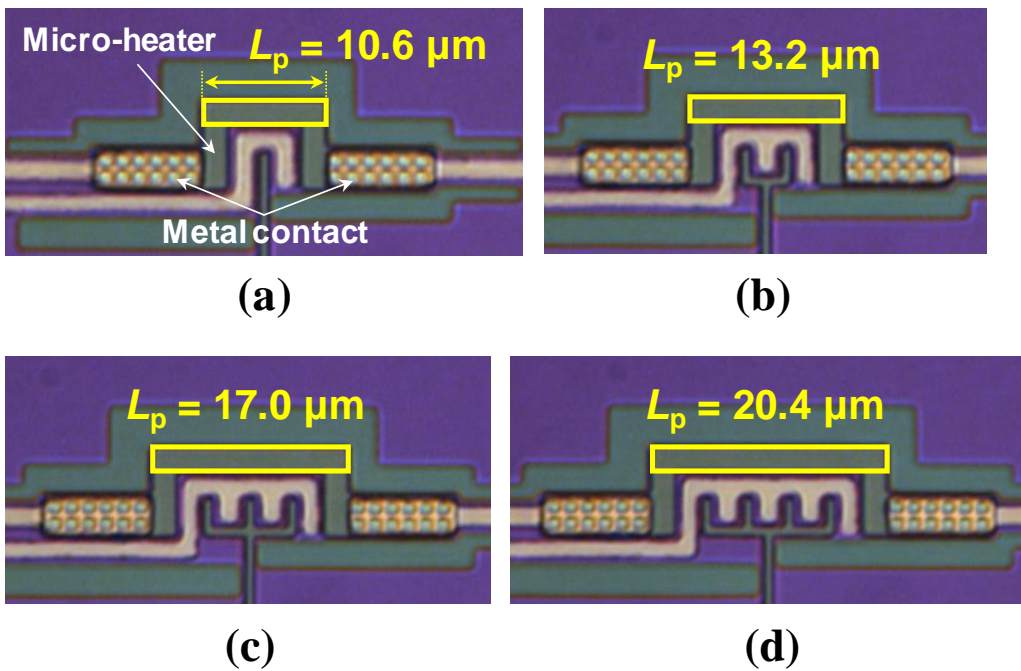


Fig. 3.1. (a)-(d) Four poly-Si micro-heaters with different lengths used to obtain the resistivity of poly-Si. The length of a portion of each poly-Si micro-heater indicated

by a yellow box is denoted as L_p .

Fig. 3.2 shows the resistance of micro-heater (R_H) versus (L_p) curve (black line), which was obtained by applying a DC bias of 1 V between the two electrodes, and the linear fit of the R_H - L_p curve (red line). From the slope of the linear fit, a poly-Si resistance per 1 μm of 54.31 $\Omega/\mu\text{m}$ was obtained. The resistivity of poly-Si (ρ_{poly}) can be calculated by:

$$\rho_{\text{poly}} = \frac{R}{l} A \quad (2)$$

where R/l and A are the poly-Si resistance per unit length and the cross-sectional area of the poly-Si micro-heater ($2 \mu\text{m} \times 0.35 \mu\text{m}$). Finally, the ρ_{poly} of $3.8 \times 10^{-3} \Omega \cdot \text{cm}$ was obtained.

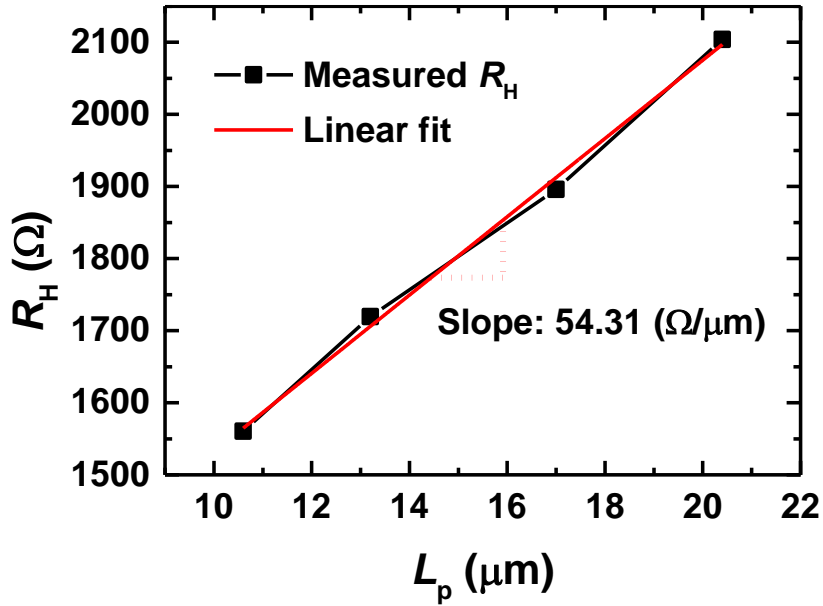


Fig. 3.2. Resistance of micro-heater (R_H) versus length of a portion of micro-heater (L_p) (black line), and the linear fit of the R_H - L_p curve (red line). A DC bias of 1 V was applied between the two electrodes to measure the currents.

3.1.2. Contact resistance extraction

By using the ρ_{poly} as obtained above, the contact resistance can also be calculated. Since the micro-heaters have a lowercase “n” shape, the total length of the poly-Si micro-heater except the metal contact region (L_{poly}) should be approximated as represented by a yellow solid line in Fig. 3.3. Then, the resistance

of the poly-Si micro-heater except the metal contact region (R_{poly}) can be calculated

by:

$$R_{poly} = \rho_{poly} \frac{L_{poly}}{A} \quad (3)$$

By using the measured R_{HS} in Fig. 3.2 and the R_{polyS} , the contact resistances (R_{cS})

of the four micro-heaters can be calculated by:

$$R_c = \frac{R_H - R_{poly}}{2} \quad (4)$$

The R_c is approximately 200Ω and the obtained R_{cS} are shown in Table 3.1.

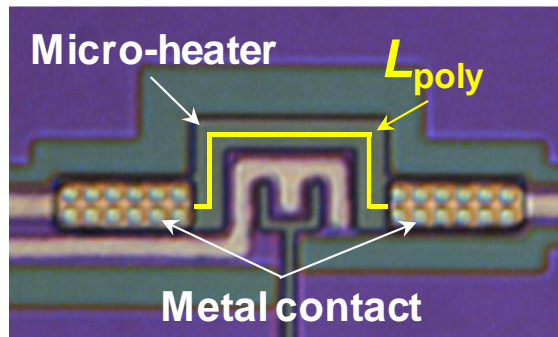


Fig. 3.3. Approximation of the total length of the poly-Si micro-heater except the metal contact region (L_{poly}).

Table 3.1. L_{polyS} , R_{polyS} , and R_{cS} of the four poly-Si micro-heaters having different lengths.

	$L_{\text{poly}} (\mu\text{m})$	$R_{\text{poly}} (\Omega)$	$R_{\text{c}} (\Omega)$
(a)	21.4	1162	199.2
(b)	24.0	1303	208.0
(c)	27.8	1510	193.1
(d)	31.2	1694	204.9

3.2. Resistance-temperature relation in poly-Si micro-heater

The electrical resistance of a material and its temperature dependence is a traditional way of classifying solids. A material with a very low resistivity (typically $< 10^{-4} \Omega \cdot \text{cm}$) that increases as the temperature increases is classified as a metal. A material with an intermediate-range resistivity (typically 10^{-3} to $10^{11} \Omega \cdot \text{cm}$) that decreases with increasing temperature is classified as a semiconductor. A material with a very high resistivity (typically $> 10^{12} \Omega \cdot \text{cm}$) that is rather independent of temperature is classified as an insulator. This classification scheme is largely

consistent with the more modern approach, which uses band theory. A final type of material is a superconductor. A superconductor is a material whose resistance is similar to that of a metal at high temperatures, but whose resistance drops to zero below a particular temperature, which is associated with a phase transition [59].

Metals and semiconductors whose resistance varies with temperature are used as resistance thermometers or thermistors [60-63], which are generally used in two ways. First, they can be used as thermometers: By measuring the resistance, the temperature of the environment can be inferred. Second, they can be used in conjunction with Joule heating (also called self-heating): If a large current is running through the resistor, the resistor's temperature rises and therefore its resistance changes. Therefore, these components can be used in a circuit-protection role similar to fuses, or for feedback in circuits, or for many other purposes. In general, self-heating can turn a resistor into a nonlinear and hysteretic circuit element [64].

If the temperature T does not vary too much, the relation between resistance of material and temperature is expressed as below (a linear approximation):

$$R(T) = R_0 [1 + \alpha(T - T_0)] \quad (5)$$

where α is called the temperature coefficient of resistance (TCR), T_0 is a fixed reference temperature, and R_0 is the resistance at temperature T_0 . The parameter α is an empirical parameter fitted from measurement data. The temperature coefficient is typically 3×10^{-3} to $6 \times 10^{-3} \text{ K}^{-1}$ for metals near room temperature. It is usually negative for semiconductors and insulators, with highly variable magnitude [65].

In general, intrinsic semiconductor resistivity decreases with increasing temperature. The electrons are bumped to the conduction energy band by thermal energy, where they flow freely, and in doing so leave behind holes in the valence band, which also flow freely. The electric resistance of a typical intrinsic semiconductor decreases exponentially with temperature [55,65,66]:

$$\rho = \rho_0 e^{-aT} \quad (6)$$

Doped semiconductors ($\leq 10^{18} \text{ cm}^{-3}$) have a far more complicated temperature profile as shown in Fig. 3.4 [65]. As temperature increases starting from absolute

zero (ionization range), thermal energy from increased temperature excites dopant electrons from the valence to the conduction band and the free electron concentration increases. Thus, the resistance decreases with the increase of temperature, and at this time, the semiconductor has a negative TCR. In the intermediate range, since the carrier concentration is equal to the doping concentration (N_d), the resistance depends on the mobility. At high temperatures, the intrinsic carrier concentration (n_i) is much larger than N_d , resulting from the thermal generation. Therefore, the resistance decreases with the increase in temperature.

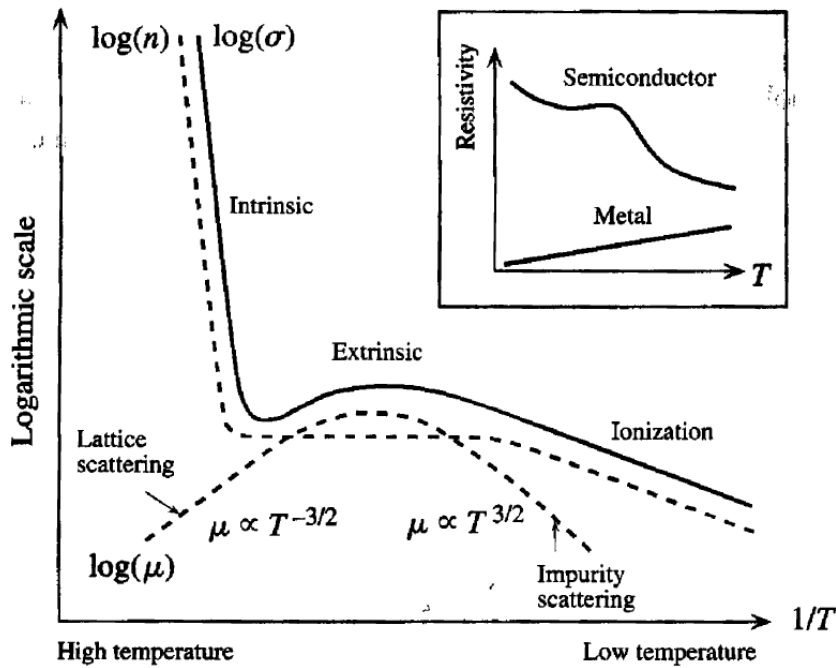


Fig. 3.4. Temperature (T) dependence of electrical conductivity (σ) for a doped semiconductor (n -type) [65]. n and μ represent carrier concentration and mobility of the semiconductor, respectively.

If the semiconductor is heavily doped with impurities, the carrier concentration is so large, typically 10^{19} - 10^{20} cm^{-3} . Such a semiconductor, which is called a degenerate semiconductor, acts more metal-like than semiconductor-like. Assume that an n -type semiconductor is a degenerate semiconductor which is heavily doped

with the donors. The donor atoms become so close to each other that their orbitals overlap to form a narrow energy band that overlaps and becomes part of the conduction band (CB). Therefore, E_c is slightly shifted down and the valence electrons from the donors fill the band from E_c . The Fermi level (E_F) is above E_c and thus the majority of the states between E_c and E_F are full of electrons as shown in Fig. 3.5 [65].

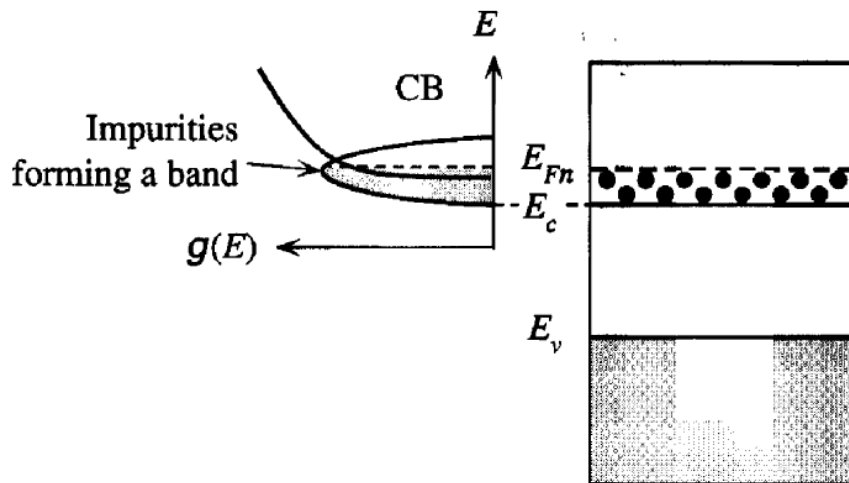


Fig. 3.5. Heavily n -type doped semiconductor [65]. A band overlapping the CB is formed by large number of impurities.

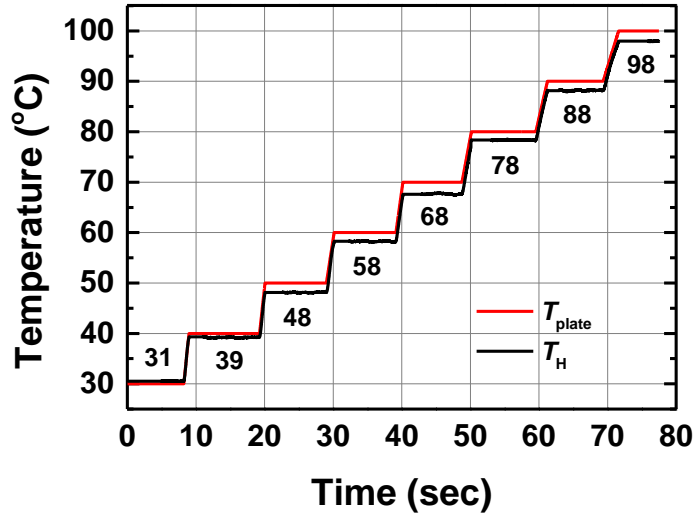
For high doping levels ($\geq 10^{19} \text{ cm}^{-3}$), the thermal generation of electrons from the donors rarely affects the resistance due to the large number of electrons already in the conduction band. Not all dopants are able to become ionized, and the carrier concentration eventually reaches a saturation. At these doping levels, the temperature-dependent behavior is dominated by mobility. At high temperatures, resistance increases with the increase in temperature [66-72] because the scattering effect of free electrons or holes by the thermal vibrations of impurities, which is called a lattice scattering, dominates. This property of a heavily-doped semiconductor is very similar to that of metal [65,73,74]. On the other hand, as temperature decreases to absolute zero, the thermal energy of the free carriers decreases and the electrostatic force between the carriers and the impurities increases, resulting in the increase in resistance. This is called an impurity scattering, which is a semiconductor-like behavior. Therefore, a U-shaped resistance versus temperature curve is obtained [67]. The temperature, at which the sign of TCR in a U-shaped curve changes from negative to positive, is called a critical point, which moves in the negative direction of the temperature axis as the doping concentration

of a heavily doped semiconductor increases [67].

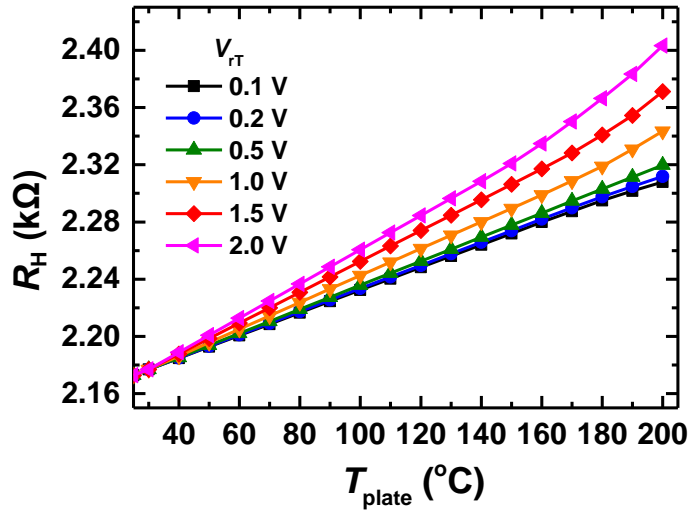
3.3. Measurement methods and results

As mentioned in Section 3.2, the temperature of poly-Si can be obtained from its resistance measured by itself. Prior to measuring the temperature of poly-Si micro-heater (T_H), Fig. 3.6(a) shows the change in T_H as the temperature of hot plate (T_{plate}) rises from 30°C to 100°C. The T_H s were measured by using infrared thermal microscopy [75,76]. The difference between T_{plate} and T_H is $\sim 2^\circ\text{C}$ and all T_H data obtained in this work are calibrated. Fig. 3.6(b) shows heater resistance (R_H) versus T_{plate} as a parameter of the bias for reading the temperature (V_{rT}). In Fig. 3.6(b), the R_H increases with increasing T_{plate} , which is characteristic of heavily-doped poly-Si micro-heater as explained in Section 3.2. The slope of R_H - T_{plate} curve becomes steeper as the V_{rT} applied to the heater increases from 0.5 to 2.0 V and the curve becomes more nonlinear with increasing V_{rT} at $> 150^\circ\text{C}$. The reason is that the increase of V_{rT} leads to the increase of Joule heating, so that T_H rises. In this work, the $|V_{\text{rT}}|$ of 0.5 V or less is applied to read the T_H , because Joule heating is negligible.

Using the calibrated R_H versus T_H , the T_H can be extracted from the measured R_H after the V_H pulse (> 1 V) is applied to the heater at a fixed T_{plate} .



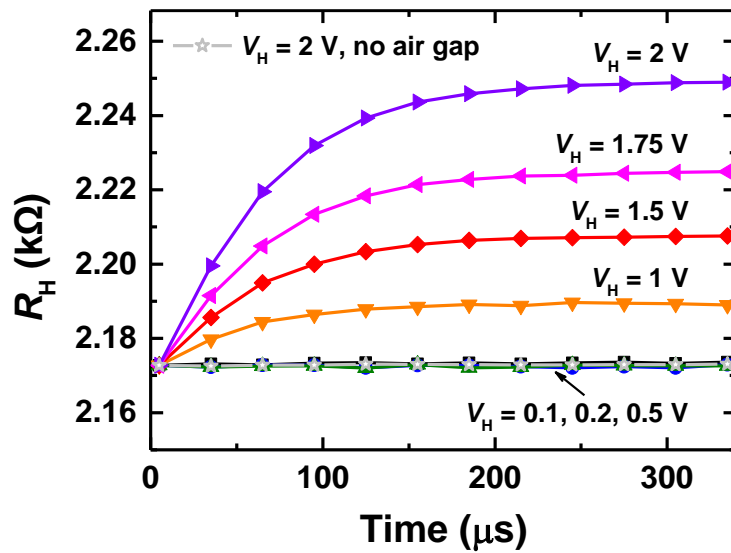
(a)



(b)

Fig. 3.6. (a) Change in T_{H} by raising the T_{plate} from 30 to 100°C (10°C step). No bias voltage is applied to the micro-heater. The T_{H} is measured by using infrared thermal microscopy [31]. (b) $R_{\text{H}}-T_{\text{plate}}$ as a parameter of V_{rT} .

Fig. 3.7(a) and (b) depict the transient R_H and T_H behaviors as a function of V_H , respectively, during the heating of micro-heater. Fig. 3.7(c) shows the measurement method to obtain R_H during the heating. After a 500 μs -long V_H pulse was applied at $t = 0$ s, the R_H s were measured at intervals of 30 μs . In Fig. 3.7(a) and (b), the R_H and the T_H are saturated when the heat generated by the V_H above 1 V is equal to the heat dissipated. It was confirmed that a pulse width of V_H longer than 200 μs is required to reach the maximum T_H at $V_H = 2$ V.



(a)

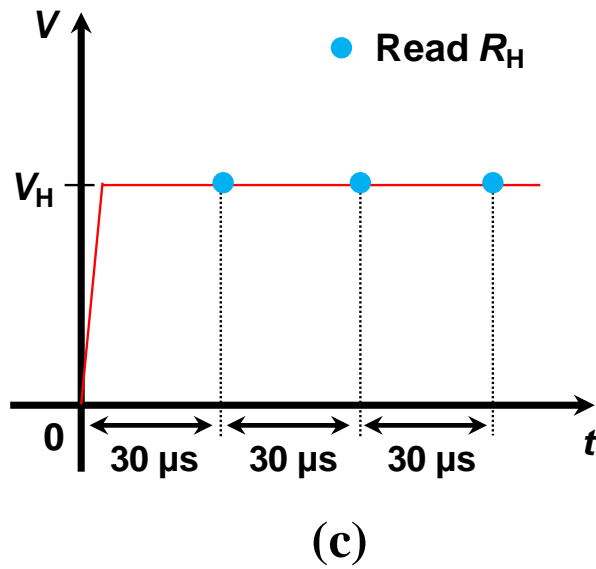
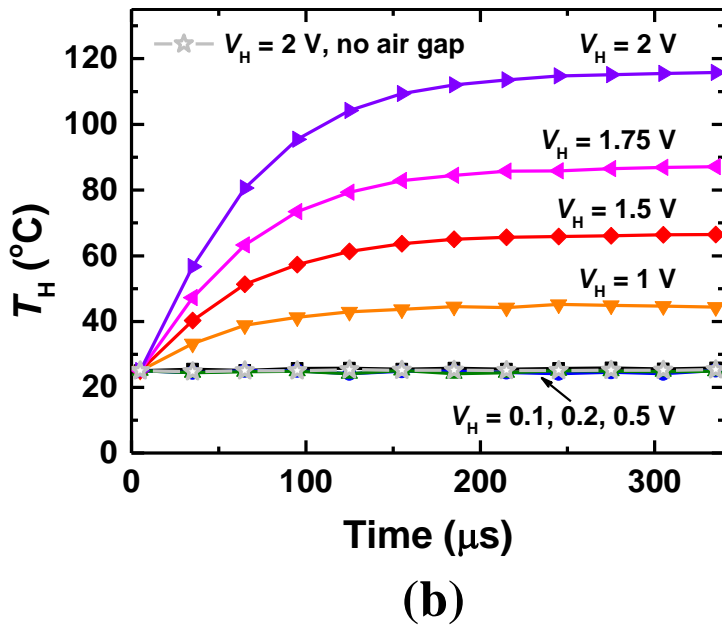
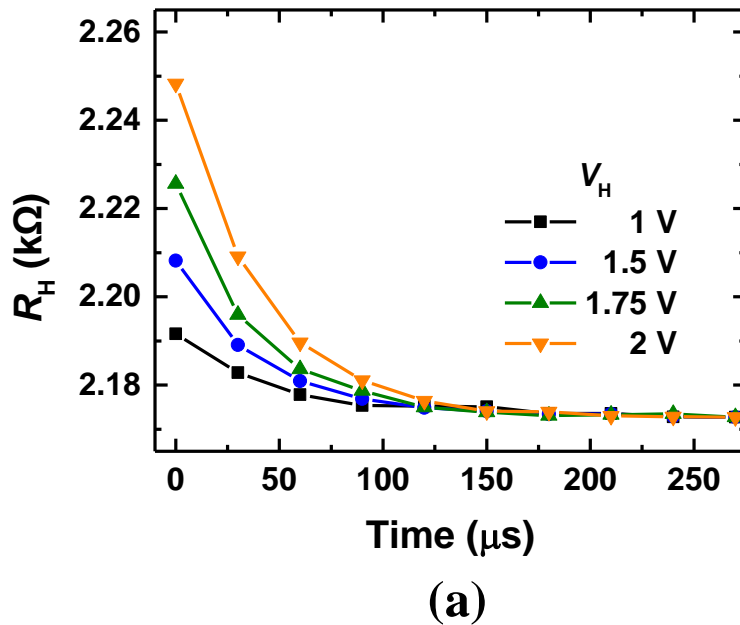
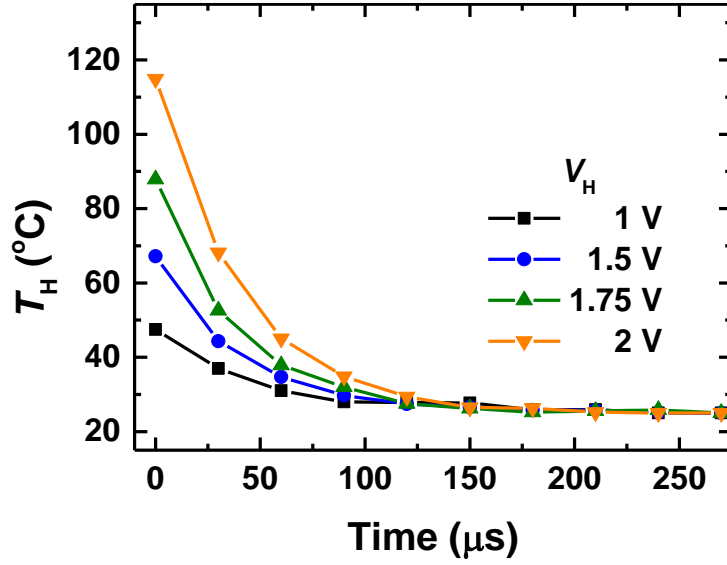


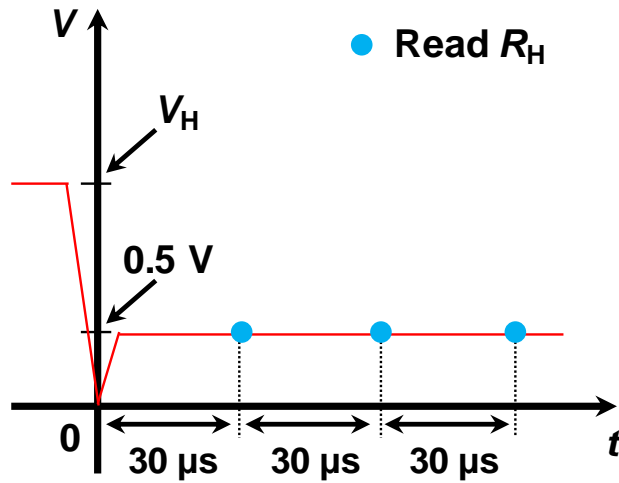
Fig. 3.7. Transient behaviors of (a) R_H and (b) T_H as a function of V_H [31], and (c) a measurement method for obtaining R_H after a 500 μs -long V_H pulse is applied at $t = 0$ s.

Fig. 3.8(a) and (b) depict the transient R_H and T_H behaviors as a function of V_H , respectively, during the cooling of micro-heater. Fig. 3.8(c) shows the measurement method to obtain R_H during the cooling. After a 500 μs -long V_H pulse was turned off at $t = 0$ s, a 500 μs -long V_{rT} pulse of 0.5 V was applied to read the R_H at intervals of 30 μs . According to Fig. 3.6(b) and 3.7(b), the V_{rT} pulse of 0.5 V was chosen because the V_{rT} pulse should not affect the T_H during the cooling. It was found that a 150 μs is sufficient to cool down the heated heater with an applied 2 V of V_H to 25°C.





(b)



(c)

Fig. 3.8. Transient behaviors of (a) R_H and (b) T_H as a function of V_H [31], and (c) a measurement method for obtaining R_H after a 500 μs -long V_H pulse is turned off at $t = 0$ s.

Fig. 3.9(a) and (b) display maximum value of T_H ($T_{H,max}$) versus frequency as parameters of V_H (@ 50% of duty cycle) and duty cycle (@ $V_H = 2$ V), respectively. The T_H data are obtained by using infrared thermal microscopy. In Fig. 3.9(a), the $T_{H,max}$ s at frequency below 1 kHz are kept at the same value due to the reason that the pulse width of V_H is long enough to reach the maximum temperature, as displayed in Fig. 3.7(a) and (b). In Fig. 3.9(b), the $T_{H,max}$ increases as the duty cycle of V_H pulse increases, since the pulse width becomes longer at a certain frequency.

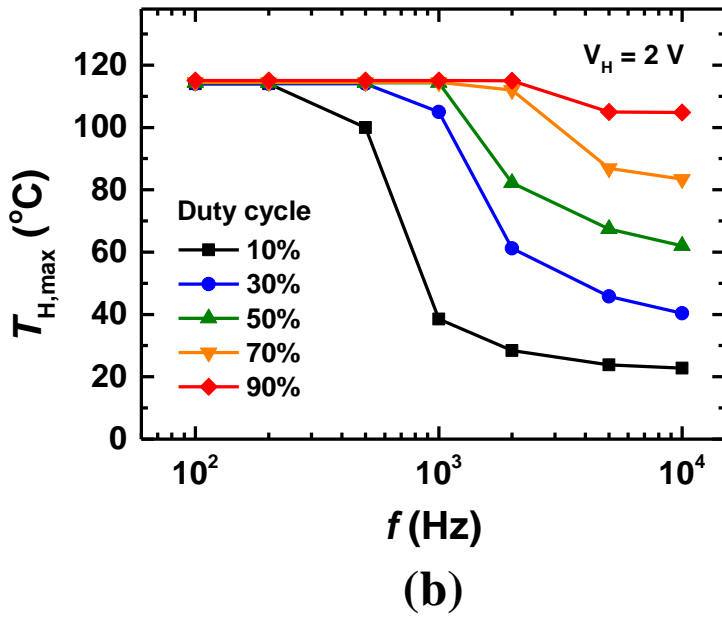
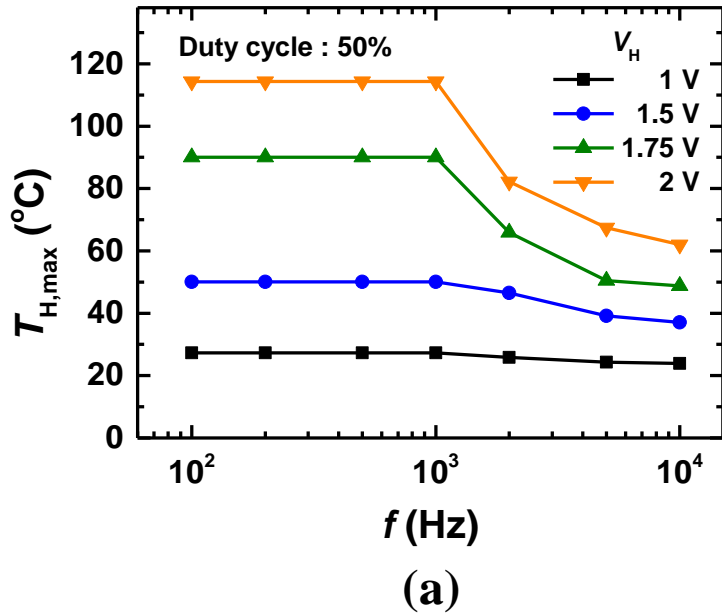


Fig. 3.9. $T_{H,max}$ versus frequency as a parameter of (a) V_H (50% of duty cycle) and (b) duty cycle ($V_H = 2$ V). The temperatures are obtained by using infrared thermal microscopy [31].

3.4. Temperature distribution in the fabricated gas sensor

Fig. 3.10 shows the DC I_D - V_{CG} characteristics of the gas sensor at different T_{plateS} (symbols) and the same T_{HS} as T_{plateS} by applying the V_{HS} to the heater (lines). The V_{DS} is fixed at -0.1 V. As the T_{plate} rises, the T_H also increases, as shown in Fig. 3.6(a), and the drain off-current increases due to drain-to-substrate junction leakage [77,78]. On the other hand, as the V_H increases at a fixed T_{plate} of 25°C, only the T_H of the micro-heater rises. Therefore, there is no increase in drain off-current by virtue of the FET temperature being kept at 25°C.

To demonstrate the result in Fig. 3.10, the temperature distribution data of the gas sensor is obtained by using thermorefectance microscopy in Fig. 3.11(a) and (b) [79,80]. Here, the V_H of the pulse applied to the heater is 2 V. The distance between the micro-heater and the FET is $\sim 20 \mu\text{m}$. In Fig. 3.11(b), no temperature increase is observed in the vicinity of the FET. It is verified that heating by applying V_H up to 2 V to the heater has no influence on the FET operation of the gas sensor.

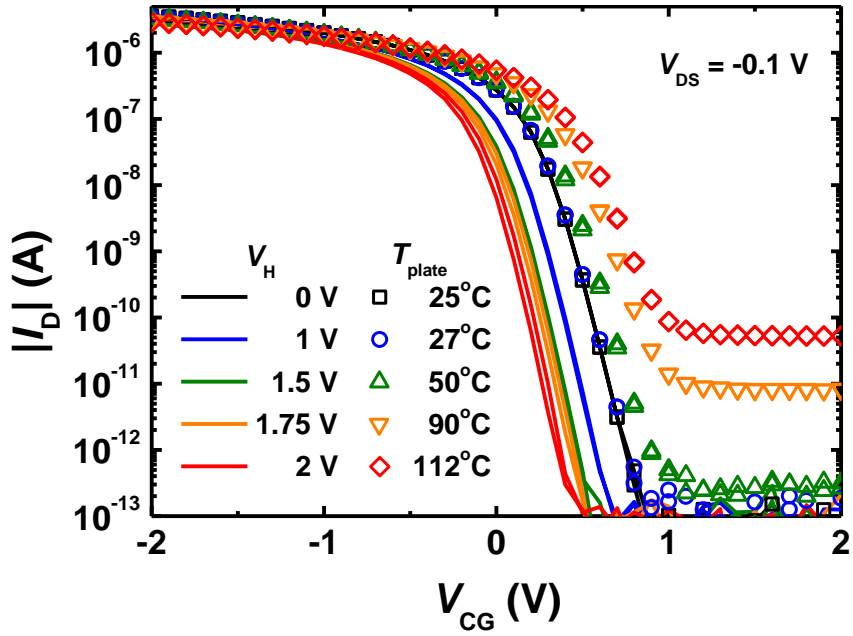


Fig. 3.10. I_D - V_{CG} curves as a parameter of V_H (line) and T_{plate} (symbol) measured by DC method. The T_{HS} at V_{HS} of 0, 1, 1.5, 1.75 and 2 V are 25, 27, 50, 90 and 112 $^{\circ}\text{C}$, respectively [31].

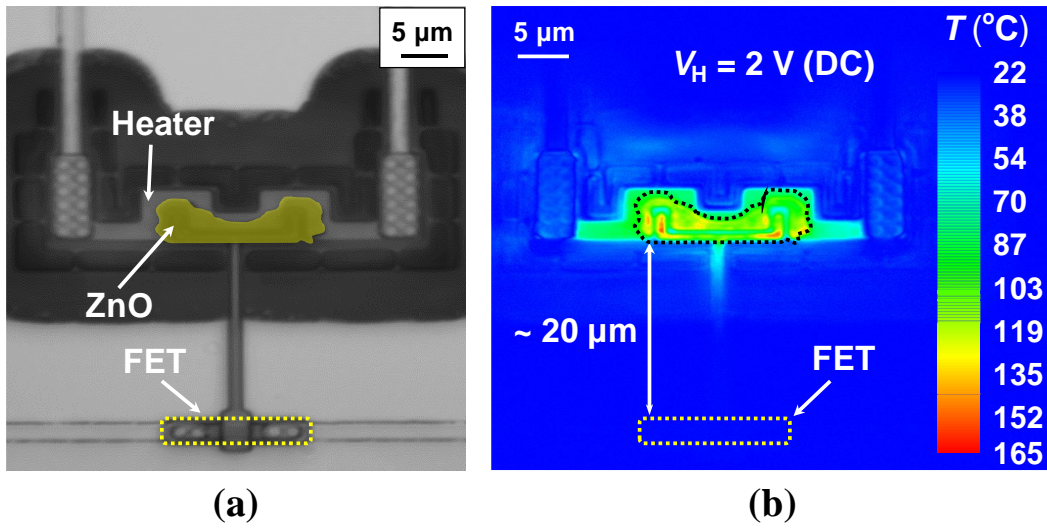


Fig. 3.11. (a) Optical microscopic image and (b) temperature distribution image of the gas sensor. The temperature distribution image is obtained by using thermoreflectance microscopy. The distance between the micro-heater and the channel is $\sim 20 \mu\text{m}$. A bias voltage of 2 V is applied to the micro-heater [31].

Chapter 4

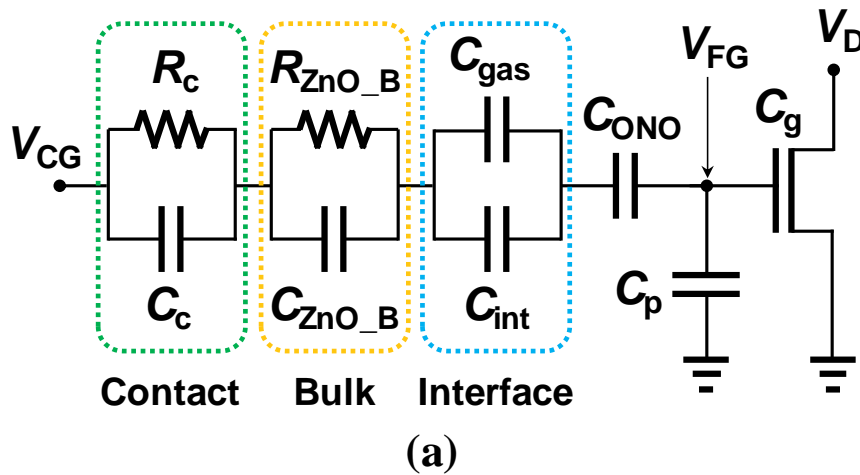
Gas-sensing characteristics

4.1. Sensing mechanism

4.1.1. Equivalent circuit of the fabricated gas sensor

The equivalent circuit of the Si FET-type gas sensor was previously studied in [81]. In [81], the Si FET-type sensor platform, the sensing material, and the deposition method of the sensing material were the same as used in this study. As shown in Fig. 4.1(a), the gate part of the device between the CG and the FG nodes is composed of the three components in series: contact, bulk, and interface. R_c and C_c stand for contact resistance and capacitance between the CG electrode and the sensing layer, respectively. R_{ZnO_B} and C_{ZnO_B} are resistance and capacitance of the bulk region of the sensing layer, respectively. The depletion capacitances changed by gas adsorption and CG bias are denoted as C_{gas} and C_{int} , respectively. The carrier concentration of the ZnO sensing material is as high as $3 \times 10^{18} \text{ cm}^{-3}$. Therefore, the metal contact on the sensing layer can be considered to be ohmic-like, which is

demonstrated by the I - V characteristic of a resistor-type gas sensor, as shown in Fig. 4.1(b), fabricated on the same wafer where the Si FET-type gas sensor was also fabricated. By considering the ohmic-like contact, C_c and C_{ZnO_B} are considered to be open-circuited in DC or low-frequency operation. Then, the series resistance of R_c and R_{ZnO_B} and the parallel capacitance of C_{gas} and C_{int} are denoted as R_{CG} and C_{CG} , respectively, as shown in Fig. 4.1(c).



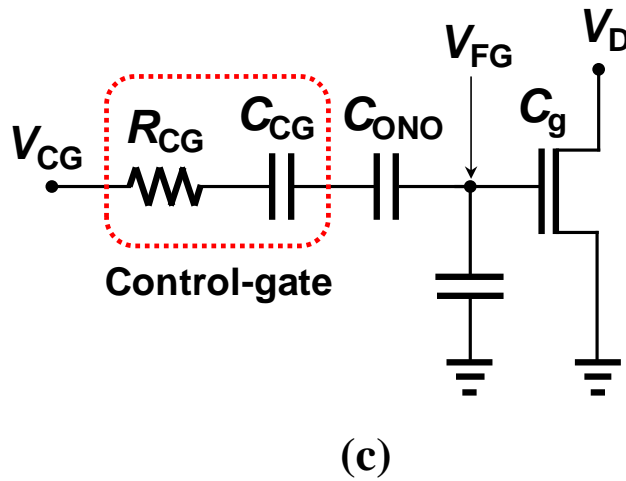
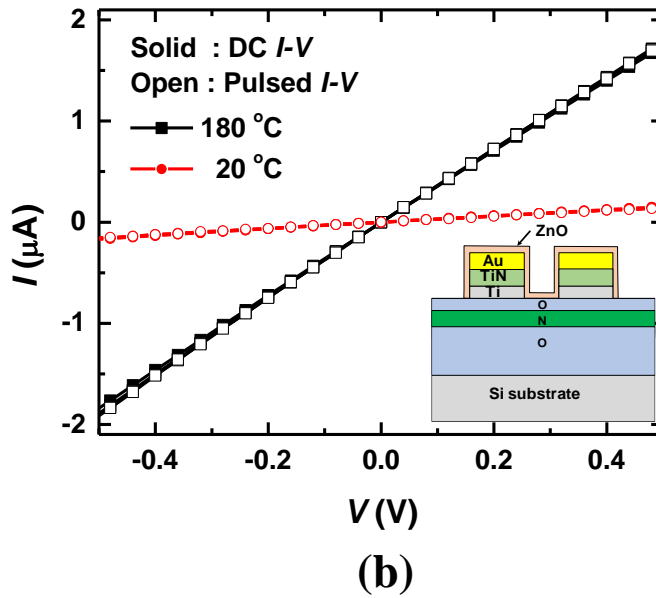


Fig. 4.1. (a) Equivalent circuit of the Si FET-type gas sensor. (b) I - V characteristic of the resistor-type gas sensor measured at 20°C and 180°C . The inset depicts a schematic cross-sectional view of the resistor-type sensor. (c) Simplified equivalent circuit [81].

The coupling ratio between CG and FG (γ) can be obtained in DC or low frequency operation as follows [81]:

$$\gamma = \frac{(C_{CG}^{-1} + C_{ONO}^{-1})^{-1}}{(C_{CG}^{-1} + C_{ONO}^{-1})^{-1} + C_g + C_p} \quad (7)$$

C_{ONO} , C_g , and C_p are the ONO layer, the gate oxide, and the parasitic capacitances, respectively. As in Eq. (7), γ is a function of C_{CG} , which changes when the gas reaction on a sensing material occurs. The threshold voltage (V_{th}) is a parameter of band bending (ϕ_b) at the surface of the sensing layer, which also changes due to the gas reaction. The change of γ or V_{th} finally changes the drain current of the Si FET-type gas sensor (I_D). In other words, the I_D is a function of γ and V_{th} . In this dissertation, nitrogen dioxide (NO_2) and hydrogen sulfide (H_2S), which are known as an oxidizing and a reducing gases, respectively, were used as target gases for gas-sensing experiments.

Fig. 4.2 shows the schematic energy band diagram of the Si FET-type gas sensor under flat band condition. Φ_{CG} , Φ_{ZnO} , Φ_{FG} , and Φ_{Si} stand for work functions

of CG, ZnO film, FG, and Si substrate, respectively. χ_{ZnO} , and χ_{Si} represent electron affinities of ZnO film and Si substrate, whose values are ~ 4.35 eV [82] and 4.05, respectively. Since the doping concentrations of poly-Si FG and Si substrate are $\sim 10^{21}$ and $\sim 10^{16}$ cm^{-3} , the Φ_{FG} and Φ_{sub} are ~ 4.05 and ~ 4.26 eV, respectively. It can be considered that $\Phi_{\text{ZnO}} \approx \chi_{\text{ZnO}}$ because the carrier concentration of ZnO is sufficiently high. The Φ_{CG} can be considered as the work function of Au ($\Phi_{\text{CG}} = \sim 5.1$ eV). Based on the information in Fig. 4.2, the sensing mechanism will be explained as follows.

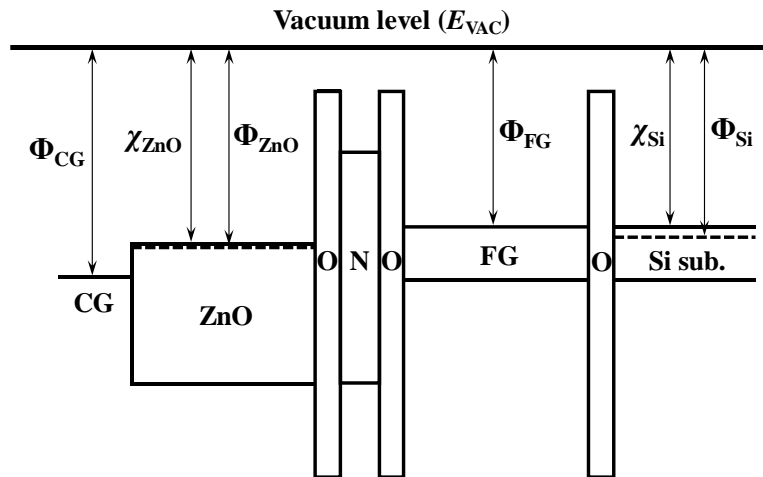


Fig. 4.2. Schematic energy band diagram of the gas sensor under flat band condition.

It was assumed that there are no charges in the oxide, nitrides, and interfaces.

4.1.2. H₂S-sensing mechanism

In ambient air, some oxygen molecules (O₂) in air are chemisorbed at the surface of the ZnO layer by extracting electrons from the CB of ZnO due to the oxidizing property of O₂ and already exist as negative ions (O⁻, O₂⁻ or O²⁻) [47,83]. This induces the depletion and the energy band bending at the surface of metal oxide. When the sensor is exposed to H₂S, H₂S molecules chemically react with the oxygen ions. The reaction produces water (H₂O) and sulfur dioxide (SO₂) while the electrons detached from the oxygen ions are returned to the ZnO layer. This reduces the depletion width and the band bending at the interface between the ZnO layer and the ONO layer as shown in Fig. 4.3 ($\phi_{b1} > \phi_{b2}$) [84], resulting in the decrease of hole concentration of the *p*MOSFET channel ($\psi_{s1} > \psi_{s2}$). Consequently, the V_{th} negatively shifts and the $|I_D|$ of the *p*-type Si FET sensor decreases as shown in Fig. 4.4(a) and (b) [44].

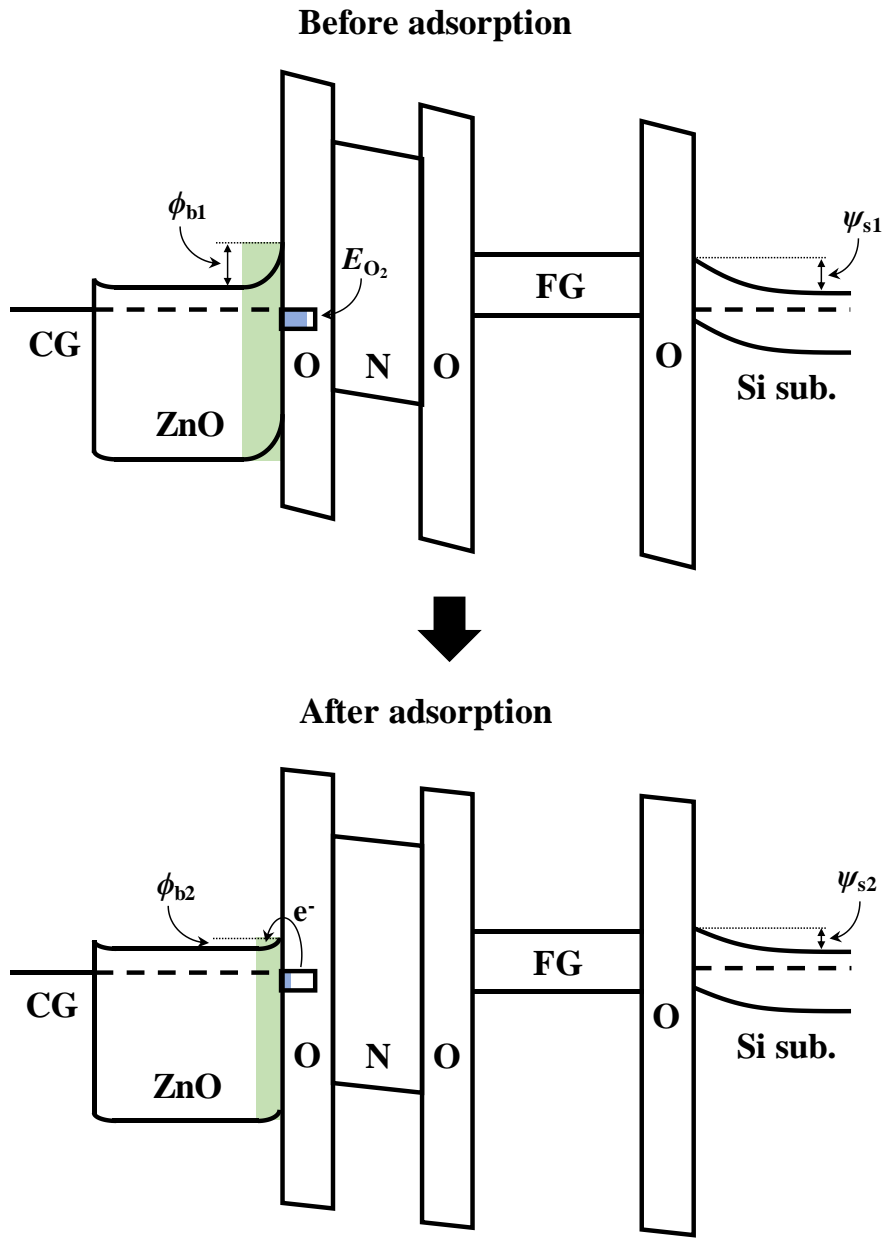


Fig. 4.3. Schematic energy band diagrams explaining the H₂S-sensing mechanism of the Si FET-type gas sensor.

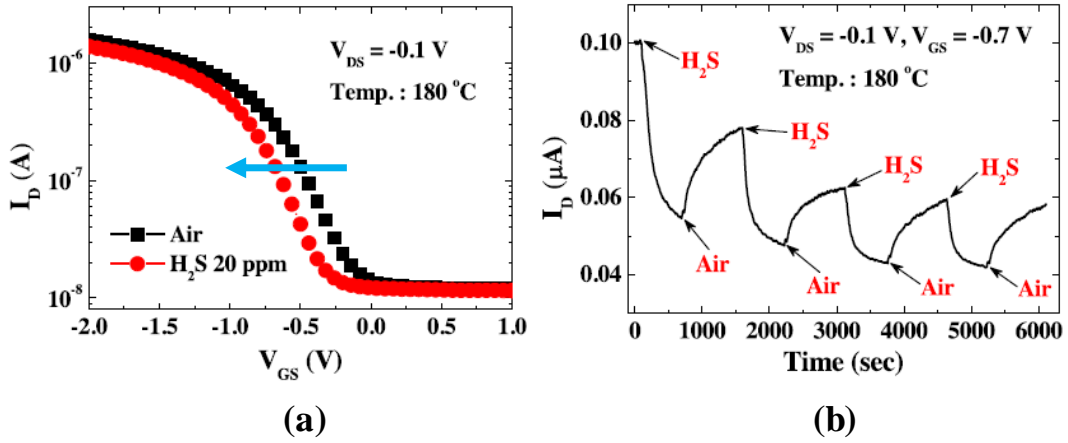


Fig. 4.4. H₂S-sensing characteristics of a Si FET-type gas sensor with a ZnO film as a sensing material [44]. (a) Negative V_{th} shift of I_D - V_{CG} curve. (b) Decrease of I_D .

4.1.3. NO₂-sensing mechanism

NO₂ molecules, which has the stronger oxidizing property than O₂, are adsorbed at the surface of ZnO by extracting electrons from ZnO and exist as negative ions (NO₂⁻), similar to O₂ chemisorption on ZnO. As depicted in Fig. 4.5, this reaction increases the depletion width and the band bending at the interface between the ZnO layer and the ONO layer ($\phi_{b1} < \phi_{b2}$) [85], resulting in the increase of hole concentration of the *p*MOSFET channel ($\psi_{s1} < \psi_{s2}$). Finally, the V_{th} positively shifts and the $|I_D|$ increases as shown in Fig. 4.6(a) and (b) [44].

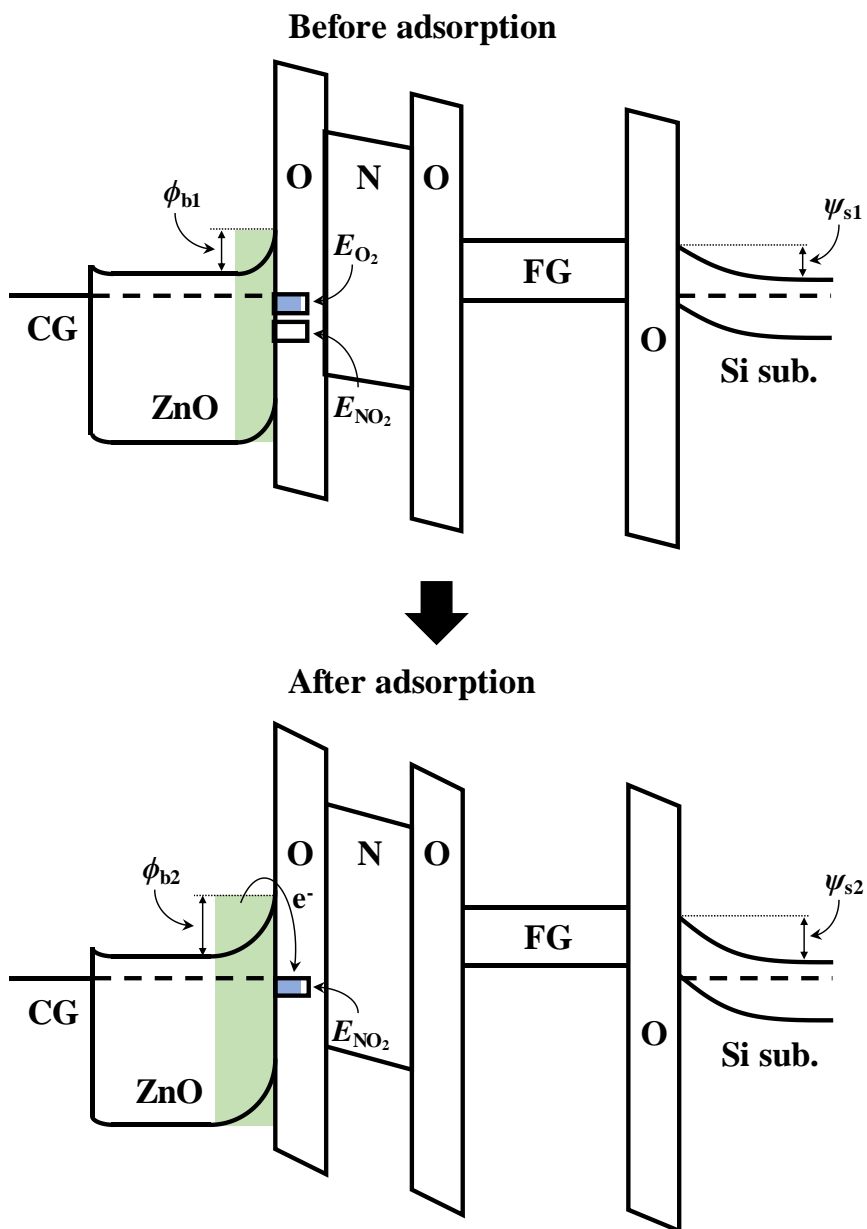
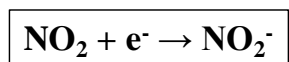


Fig. 4.5. Schematic energy band diagrams explaining the NO_2 -sensing mechanism of the Si FET-type gas sensor.

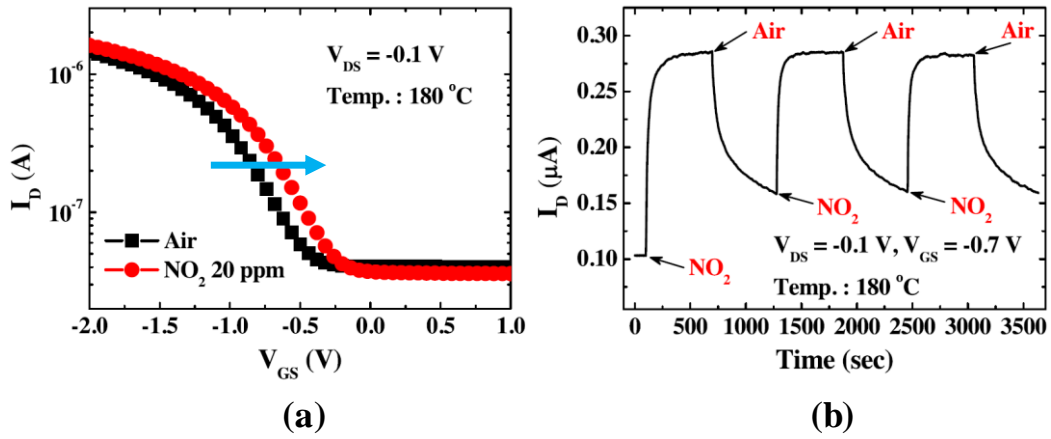


Fig. 4.6. NO_2 -sensing characteristics of a Si FET-type gas sensor with a ZnO film as a sensing material [44]. (a) Positive V_{th} shift of I_D - V_{CG} curve. (b) Increase of I_D .

4.2. Measurement setup

Fig. 4.7 illustrates the experimental setup for gas-sensing measurement. The measurements were carried out by using a probe station for gas-sensing equipped with a gas chamber, gas inlet and outlet. The fabricated gas sensor was placed in the gas chamber. Three pulse signals were used and applied to the CG, the drain, and the micro-heater. Fig. 4.8 indicates an operation scheme adopted for gas-sensing measurement. In heating period, V_H are applied to the micro-heater with a pulse width of t_H while pre-bias (V_{pre}) is applied to the CG [31]. In read period,

drain bias (V_{rDS}) is synchronized with V_{rCG} for a pulse width of t_{read} . All the gas-sensing measurements in this work were done at fixed V_{rCG} and V_{rDS} of -0.1 V and a frequency of 1 kHz in linear region of the FET-type gas sensor.

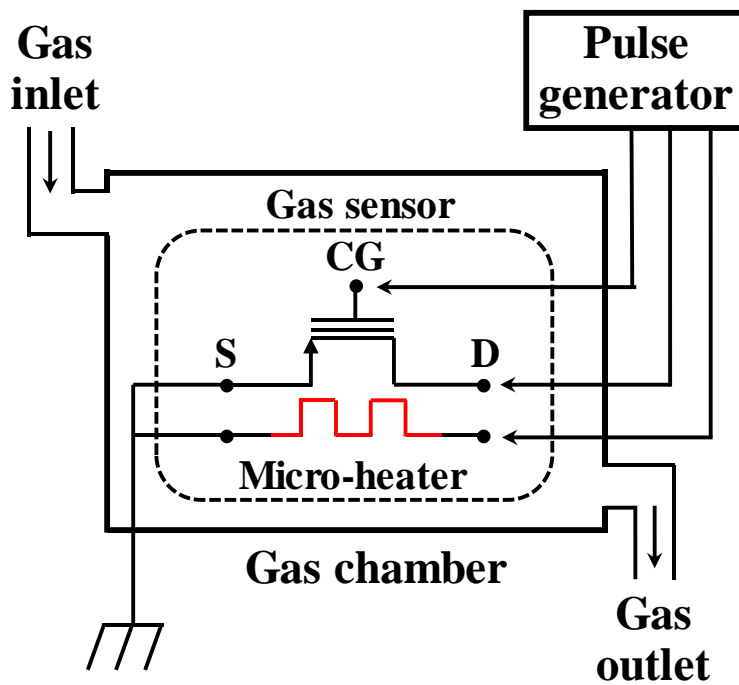


Fig. 4.7. Experimental setup for gas-sensing measurement. The three generated pulse signals are applied to the CG, the drain and the micro-heater [31].

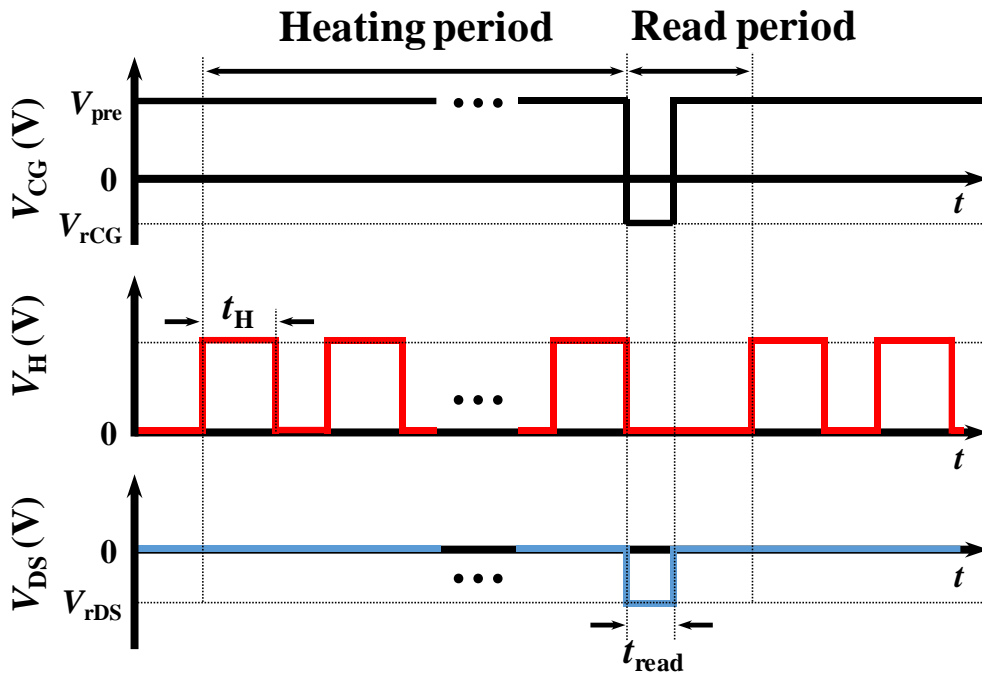
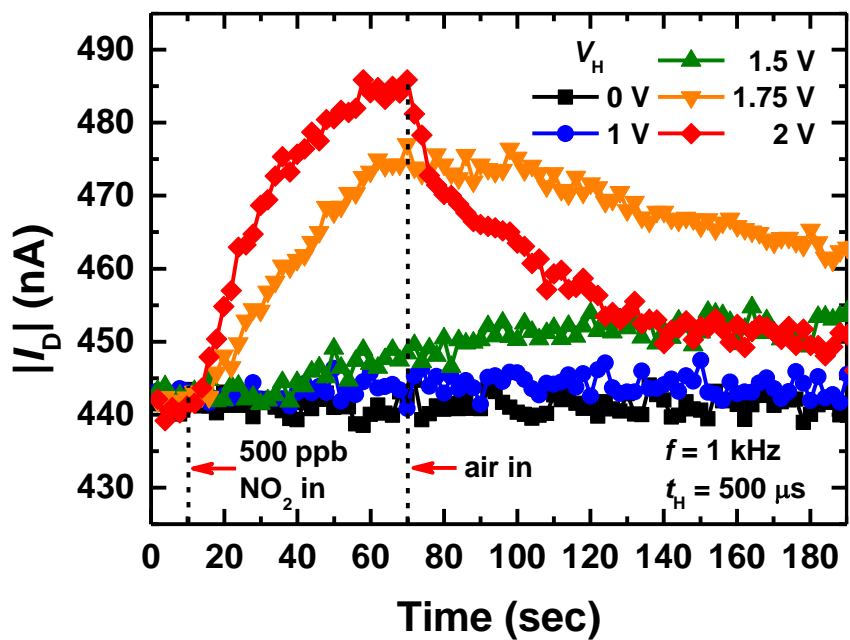


Fig. 4.8. Operation scheme of the fabricated gas sensor. V_{pre} and V_{rCG} are alternately applied to the CG. V_{rDS} is synchronized with V_{rCG} with a pulse width of t_{read} . V_H pulses are applied with a pulse width of t_H [31].

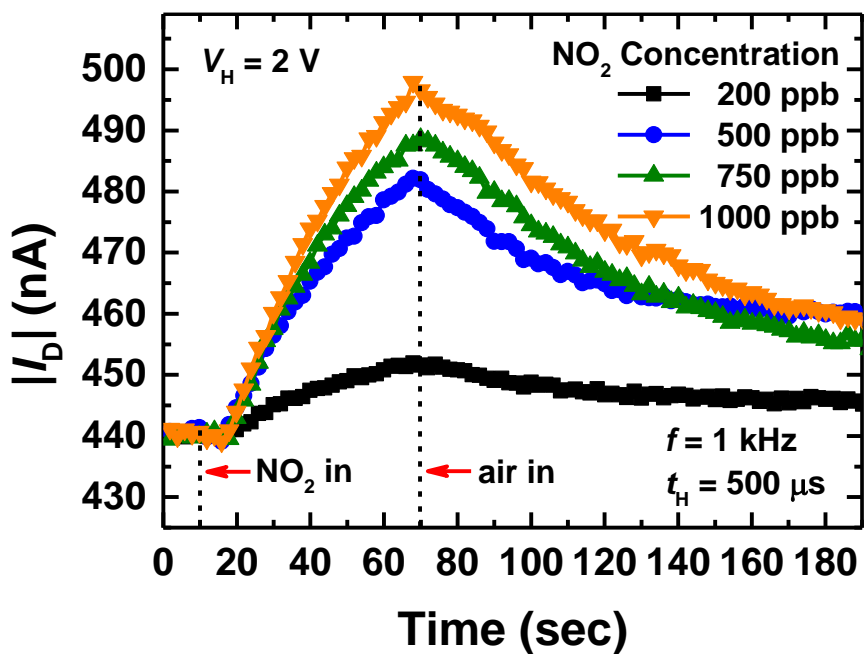
4.3. Measurement results

4.3.1. NO₂-sensing characteristics

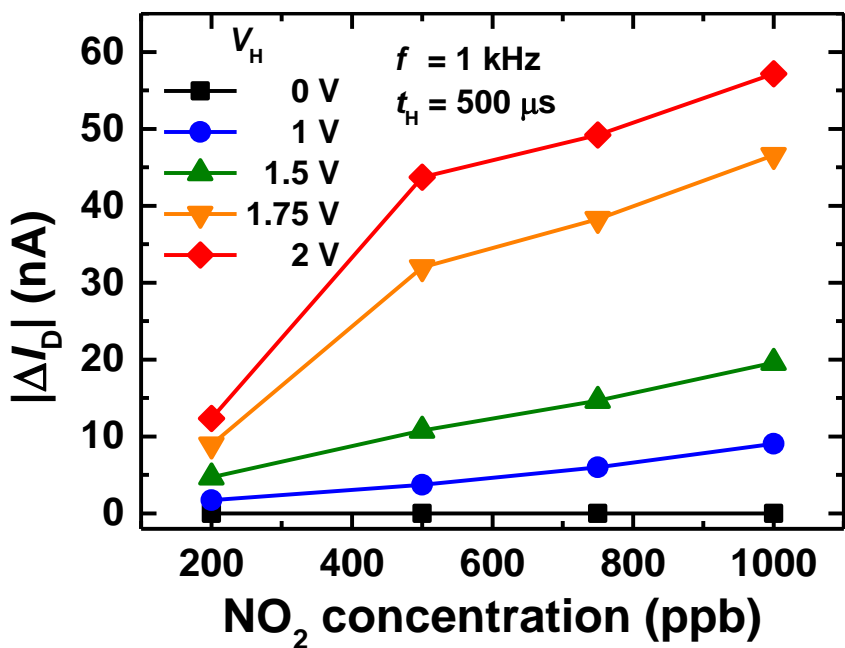
Fig. 4.9(a) and (b) show the transient I_D behaviors of the gas sensor as parameters of V_H and NO₂ concentration, respectively. In Fig. 4.9(a), the response and the recovery characteristics are improved as the V_H increases. The increase of V_H leads to the rise in T_H . NO₂ molecules then acquire more energy, resulting in higher response and faster recovery. In Fig. 4.9(b), as the NO₂ concentration increases, the $|I_D|$ increases. Sensor response versus NO₂ concentration as a parameter of V_H is shown in Fig. 4.9(c). Sensor response is obtained by the absolute value of the difference between the I_{DS} at $t = 70$ s and $t = 10$ s. At a 500 ppb NO₂ and a V_H of 2 V, the sensor response is 43.7 nA. Fig. 4.9(d) shows the transient I_D behaviors of the gas sensor as a parameter of t_H . The I_D behavior with a t_H of 500 μ s is similar to that with a t_H of 700 μ s. As shown in Fig. 3.9(b), a $T_{H,max}$ at a duty cycle of 50% is nearly the same as that of 70% at a f up to 1 kHz. Thus, using a 500 μ s-long V_H pulse is reasonable for low power operation of the gas sensor with the micro-heater. The power consumption is ~ 0.92 mW at 112°C ($V_H = 2$ V).



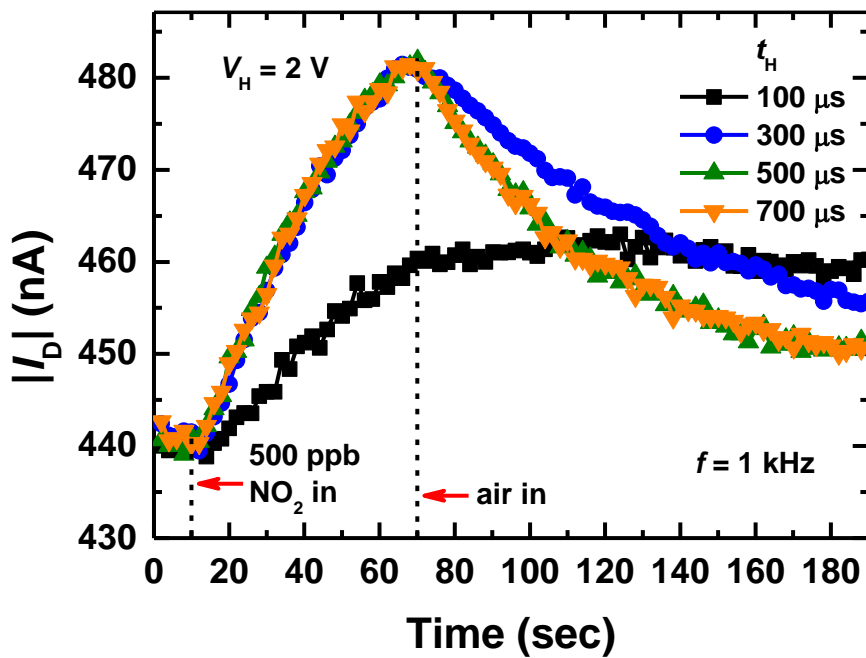
(a)



(b)



(c)

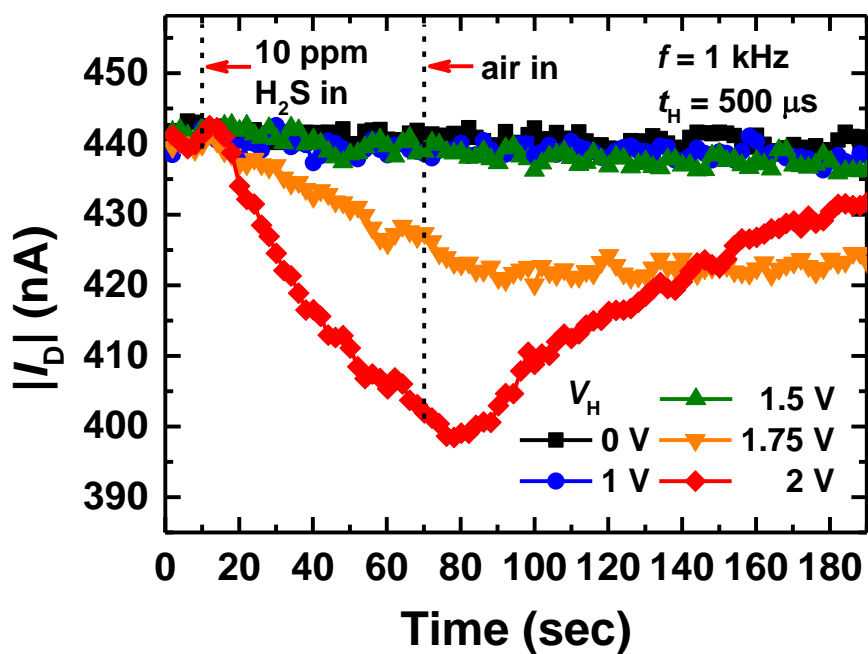


(d)

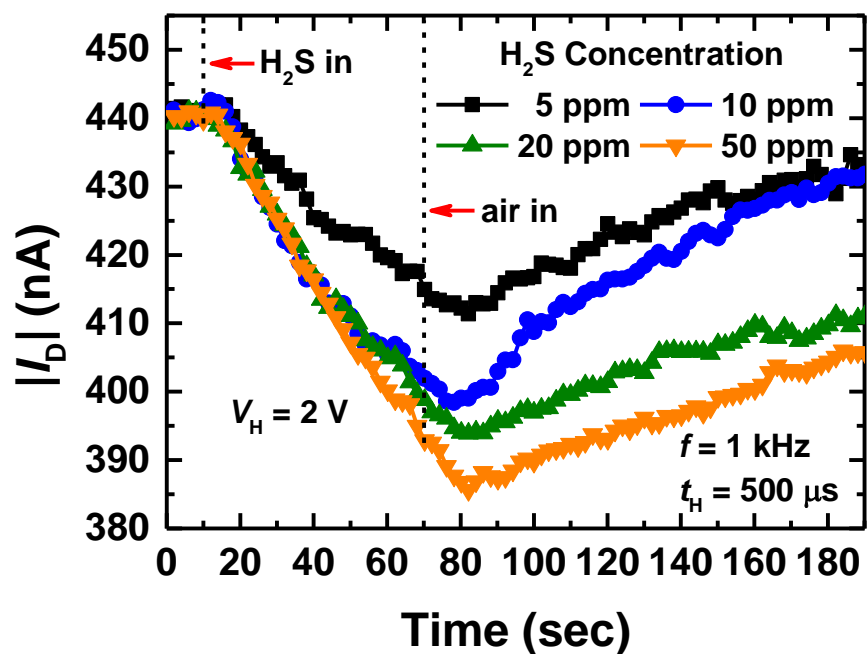
Fig. 4.9. NO₂-sensing measurement results. [31]. (a) Transient I_D behaviors to 500 ppb of NO₂ as a parameter of V_H . The t_H was 500 μ s. (b) Transient I_D behaviors as a parameter of gas concentration. The V_H and the t_H were 2 V and 500 μ s, respectively. (c) Sensor response versus NO₂ concentration as a parameter of V_H ($t_H = 500 \mu$ s). (d) Transient I_D behaviors as a parameter of t_H ($V_H = 2$ V).

4.3.2. H₂S-sensing characteristics

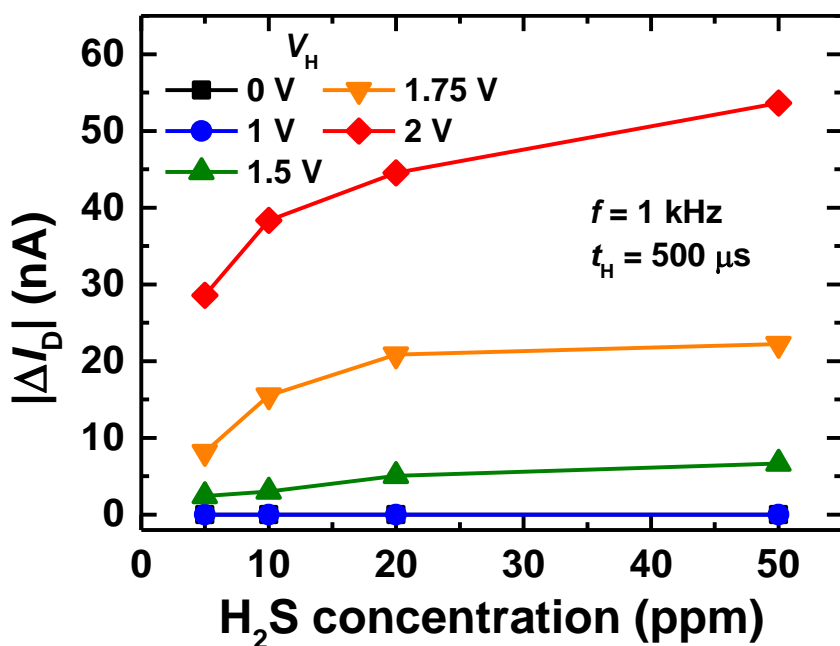
The transient responses to H₂S are illustrated as parameters of V_H , and gas concentration, in Fig. 4.10(a) and (b), respectively. As in the case of NO₂-sensing, sensor response increases as V_H or H₂S concentration increases. Fig. 4.10(c) shows sensor response versus H₂S concentration as a parameter of V_H . At a 10 ppm H₂S and a V_H of 2 V, the sensor response is 38.3 nA. Fig. 4.10(d) shows the transient I_D behaviors of the gas sensor as a parameter of t_H . From the result, using a 700 μ s-long V_H pulse is reasonable for low power operation of the gas sensor with the micro-heater.



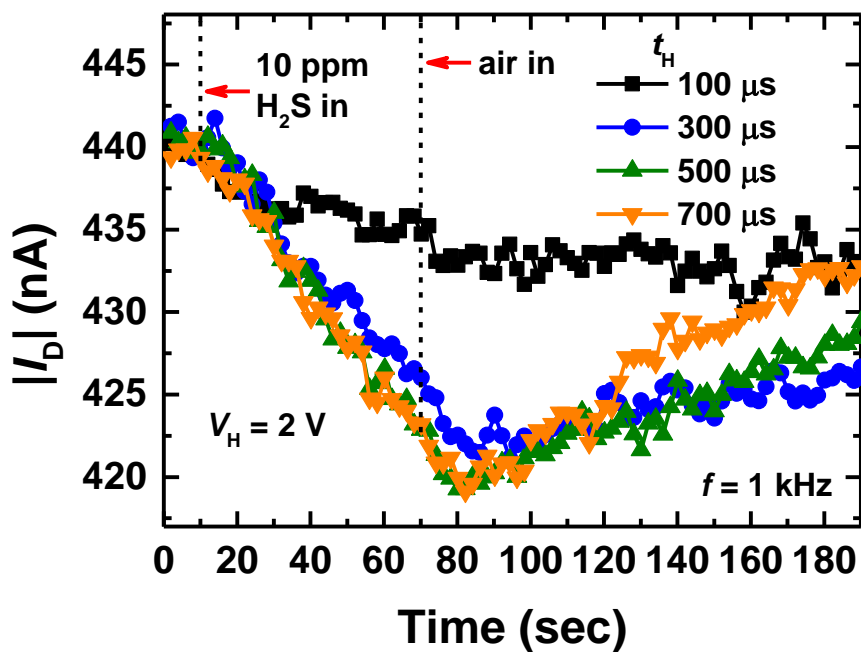
(a)



(b)



(c)



(d)

Fig. 4.10. H₂S-sensing measurement results [31]. (a) Transient I_D behaviors to 10 ppm of H₂S as a parameter of V_H ($t_H = 500 \mu\text{s}$). (b) Transient I_D behaviors as a parameter of gas concentration ($V_H = 2 \text{ V}$, and $t_H = 500 \mu\text{s}$). (c) Sensor response versus H₂S concentration as a parameter of V_H ($t_H = 500 \mu\text{s}$). (d) Transient I_D behaviors as a parameter of t_H ($V_H = 2 \text{ V}$).

4.4. Pre-bias effect on sensing performance

Prior to investigating the pre-bias effect on gas-sensing the Si FET-type sensor, the sensing mechanism is briefly explained [32,81]. Note that V_{pre} is applied to the CG during the heating period as shown in Fig. 4.8.

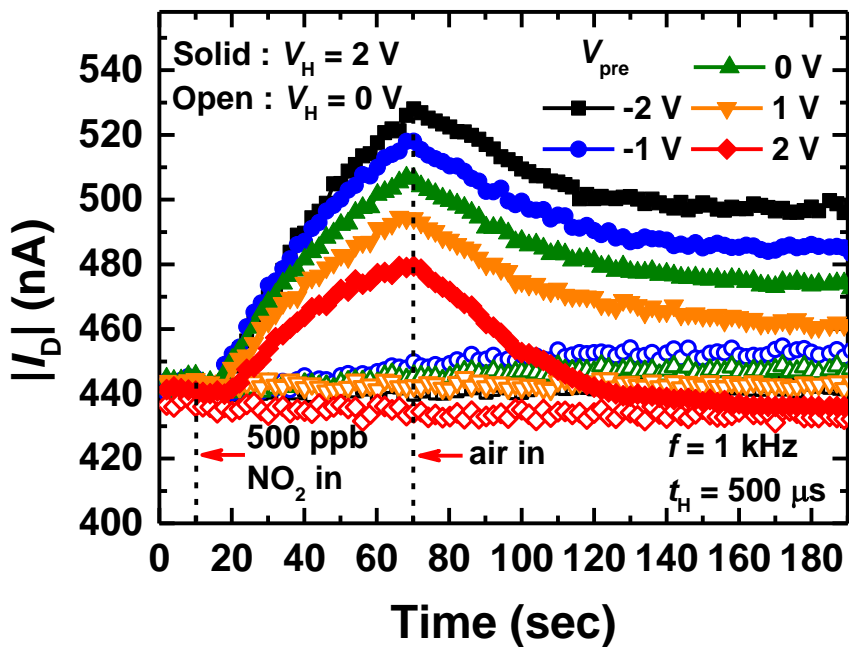
When the gas sensor is exposed to NO₂ at a $V_{\text{pre}} < 0 \text{ V}$ in the pre-bias period, the electrons in the ZnO layer are accumulated near the ZnO-ONO interface and most of the NO₂ molecules are then easily ionized at the interface. This causes the increase of band bending at the ZnO-ONO interface and therefore, the $|I_D|$ increases. In the pre-bias period with a $V_{\text{pre}} > 0 \text{ V}$, the ZnO layer near the ZnO-ONO interface is depleted and thus the NO₂ ionosorption rarely occurs at the interface. Instead, the

NO₂ molecules are ionized in the bulk region of the ZnO layer. As relatively small amounts of NO₂ molecules react, energy band bending at the ZnO-ONO interface slightly increases and finally the $|I_D|$ is increased little.

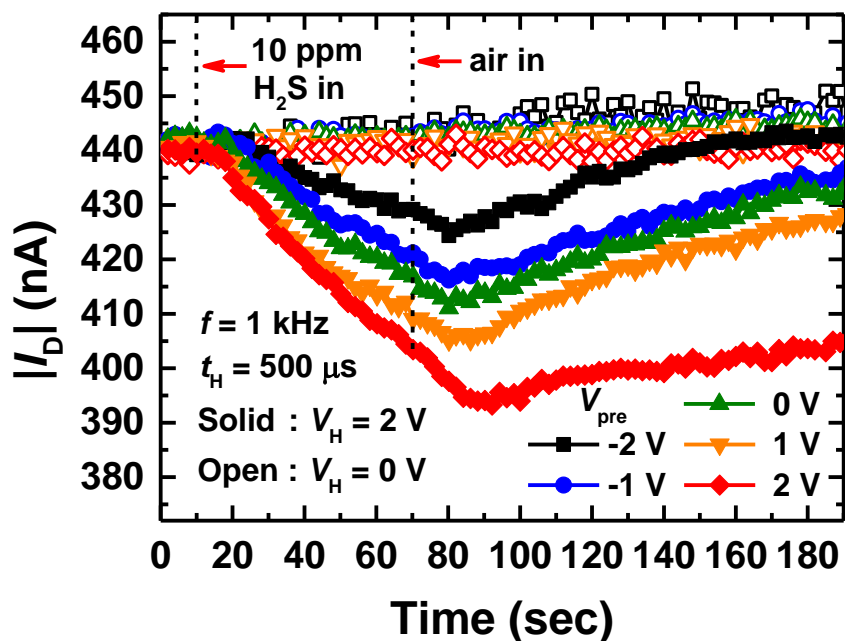
When the gas sensor is exposed to air for the recovery with a positive V_{pre} , the acceptor energy level of the NO₂⁻ ions becomes higher than the Fermi level of ZnO. Then, the electrons are easily returned from the NO₂⁻ ions to the ZnO layer and the neutralized NO₂ molecules are quickly desorbed. Therefore, the recovery time of the sensor is shortened. During the recovery with a $V_{pre} < 0$ V, on the other hand, the acceptor energy level remains lower than the Fermi level of ZnO. This means that the NO₂⁻ ions are hardly neutralized and desorbed, and consequently the recovery time is increased.

The transient responses to NO₂ and H₂S are illustrated as a parameter of V_{pre} as shown in Fig. 4.11(a) and (b), respectively. Note the responses are negligible during finite t_{read} when $V_H = 0$ V as represented by open symbols, even though V_{pre} is applied, since the gas reaction takes a long time at 25°C. In Fig. 4.11(a), the sensor response to NO₂ increases with negatively increasing V_{pre} , whereas the recovery

time is shortened with positively increasing V_{pre} [31]. Fig. 4.11(b) shows the V_{pre} effect on the sensor response to H_2S . The $|I_{\text{D}}|$ behavior with the polarity of V_{pre} is opposite to that of NO_2 .



(a)



(b)

Fig. 4.11. Pre-bias effects on the detection of NO₂ and H₂S [31]. Transient responses to (a) 500 ppb of NO₂ and (b) 10 ppm of H₂S as a parameter of V_{pre} (-2 ~ 2 V). Solid and open symbols represent the transient I_{D} behaviors at a V_{H} of 2 and 0 V, respectively ($t_{\text{H}} = 500 \mu\text{s}$, $V_{\text{rCG}} = V_{\text{rDS}} = -0.1 \text{ V}$).

4.5. Gas-sensing in stable NO₂ ambience

Fig. 4.12 indicates sensor response in 500 ppb NO₂ ambience versus total heating time ($n \times t_{\text{H}}$) where n is the number of applied heating pulses ($t_{\text{H}} = 500 \mu\text{s}$, $f = 1 \text{ kHz}$). A pulse scheme used in this measurement is explained in the inset of Fig. 4.12. Before the gas sensor started operating, 500 ppb NO₂ was injected into the gas chamber for 30 min to create the stable atmosphere. We think a $\Delta|I_{\text{D}}|$ of ~2 nA is large enough to be detected even when there is noise. Since the $\Delta|I_{\text{D}}|$ of ~2 nA needs a total heating time of ~ 10 ms, the energy consumption is estimated to be ~ 18.4 μJ .

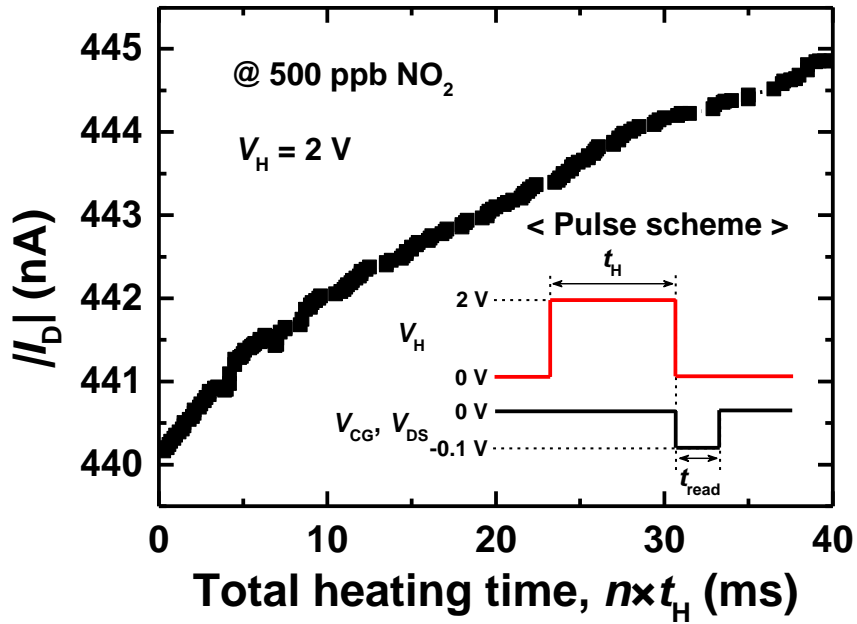


Fig. 4.12. Sensor response ($|I_D|$) in stable NO_2 ambience as a function of $n \times t_H$. The NO_2 concentration and the t_H were 500 ppb and 500 μs , respectively. The amplitude of the V_H pulse was 2 V ($V_{rCG} = V_{rDS} = -0.1 \text{ V}$, and $V_{pre} = 0 \text{ V}$).

4.6. Comparison in power consumption of micro-heaters

Compared to the micro-heaters embedded in the MEMS-based gas sensors reported by the other groups [11,12,33], the micro-heater used in this work can achieve much higher temperature with the same power consumption as displayed

in Fig. 4.13, which is attributed to the small micro-heater size and the pulse operation. The average power consumption is 0.92 mW at 112°C at a V_H of 2 V and a frequency of 1 kHz.

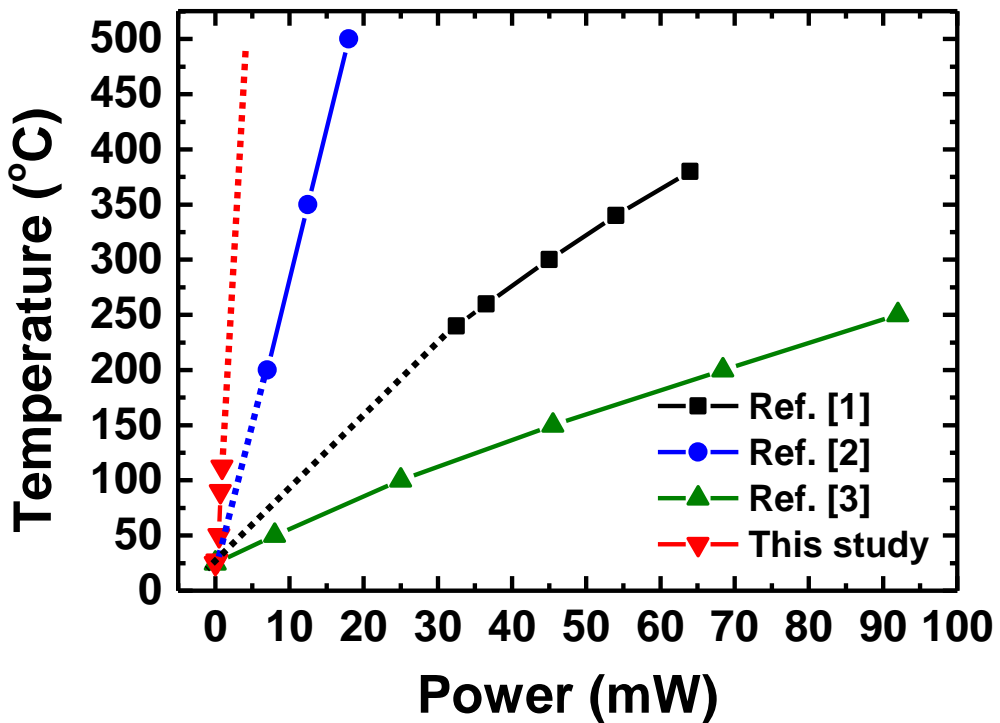


Fig. 4.13. Comparison in power consumption of the pulse-driven localized poly-Si micro-heater embedded in the Si FET-type gas sensor and the MEMS-based micro-heaters reported from the other groups.

Chapter 5

Conclusion

In this dissertation, a Si FET-type gas sensor having a localized poly-Si micro-heater has been proposed and fabricated by using conventional MOSFET process. The total six photomasks were used and the detailed explanation on the key fabrication process of the sensor was presented. The micro-heater is designed only to heat the sensing part whose area is $\sim 15 \times 5 \mu\text{m}^2$. To prevent the heat generated by the micro-heater from being dissipated, an air gap is formed under and around the sensing part. Zinc oxide (ZnO) as a sensing material was deposited by atomic layer deposition (ALD) method and characterized by X-ray diffraction (XRD) measurement.

A method to read the micro-heater temperature (T_H) by reading its resistance (R_H) was verified. The T_H of 112°C was obtained at a heating pulse bias of 2 V and the heating/cooling times of the micro-heater were $200 \mu\text{s}/150 \mu\text{s}$. T_H was then identified by infrared thermal microscopy and thermorefectance microscopy.

Nitrogen dioxide (NO_2) and hydrogen sulfide (H_2S), which are known as an oxidizing and a reducing gases, respectively, were used as target gases. The sensing mechanism was explained by using schematic energy band diagram. A pulse scheme for operating both the FET and the micro-heater of the sensor was proposed. The proposed sensor showed excellent performance in NO_2 and H_2S gas detection. As a bias for heating the micro-heater (V_H) increases, response and recovery characteristics were significantly improved. Low power consumption was achieved, which is attributed to the reduced distance between the heater and sensing material, small heater size, and pulse operation. Furthermore, the pre-bias effect was demonstrated to improve the sensing performance. It is expected that the detection of a target gas at a very low concentration will be achieved by using both micro-heater and pre-bias pulse scheme.

Bibliography

[1] E. Comini, G. Faglia, G. Sberveglieri, Z. Pan, and Z. L. Wang, "Stable and highly sensitive gas sensors based on semiconducting oxide nanobelts," *Appl. Phys. Lett.*, vol. 81, pp. 1869-1871, 2002.

[2] E. Li, Z. Cheng, J. Xu, Q. Pan, W. Yu, and Y. Chu, "Indium Oxide with Novel Morphology: Synthesis and Application in C₂H₅OH Gas Sensing," *Cryst. Growth Des.*, vol. 9, pp. 2146-2151, 2009.

[3] H. -J. Kim, J. -W. Yoon, K. -I. Choi, H. W. Jang, A. Umar, and J. -H. Lee, "Ultrasensitive and sensitive detection of xylene and toluene for monitoring indoor air pollution using Cr-doped NiO hierarchical nanostructures," *Nanoscale*, vol. 5, pp. 7066-7073, 2013.

[4] J. Shin, S. -J. Choi, I. Lee, D. -Y. Youn, C. O. Park, J. -H. Lee, H. L. Tuller, and I. -D. Kim, "Thin-Wall Assembled SnO₂ Fibers Functionalized by Catalytic Pt Nanoparticles and their Superior Exhaled-Breath-Sensing Properties for the Diagnosis of Diabetes," *Adv. Funct. Mater.*, vol. 23, pp. 2357-2367, 2013.

[5] M. Penza, R. Rossi, M. Alvisi, M. A. Signore, G. Cassano, D. Dimaio, R. Pentassuglia, E. Piscopiello, E. Serra, and M. Falconieri, "Characterization of metal-modified and vertically-aligned carbon nanotube films for functionally enhanced gas sensor applications," *Thin Solid Films*, vol. 517, pp. 6211-6216, 2009.

[6] J. Li, Y. Lu, Q. Ye, M. Cinke, J. Han, and M. Meyyappan, "Carbon nanotube sensors for gas and organic vapor detection," *Nano Lett.*, vol. 3, pp. 929-933, 2003.

[7] H. J. Yoon, D. H. Jun, J. H. Yang, Z. Zhou, S. S. Yang, and M. M. -C. Cheng, "Carbon dioxide gas sensor using a graphene sheet," *Sens. Actuators B*, vol. 157, pp. 310-313, 2011.

- [8] G. Lu, L. E. Ocola, and J. Chen, "Reduced graphene oxide for room-temperature gas sensors," *Nanotechnology*, vol. 20, p. 445502, 2009.
- [9] M. Donarelli, S. Prezioso, F. Perrozzi, F. Bisti, M. Nardone, L. Giancaterini, C. Cantalini, and L. Ottaviano, "Response to NO₂ and other gases of resistive chemically exfoliated MoS₂-based gas sensors," *Sens. Actuators B*, vol. 207, pp. 602-613, 2015.
- [10] K. Y. Ko, J. -G. Song, Y. Kim, T. Choi, S. Shin, C. W. Lee, K. Lee, J. Koo, H. Lee, J. Kim, T. Lee, J. Park, and H. Kim, "Improvement of Gas-Sensing Performance of Large-Area Tungsten Disulfide Nanosheets by Surface Functionalization," *ACS Nano*, vol. 10, pp. 9287-9296, 2016.
- [11] L. Xiao, S. Xu, G. Yu, and S. Liu, "Efficient hierarchical mixed Pd/SnO₂ porous architecture deposited microheater for low power ethanol gas sensor," *Sens. Actuators B*, vol. 255, pp. 2002-2010, 2018.
- [12] H. Long, A. Harley-Trochimczyk, T. He, T. Pham, Z. Tang, T. Shi, A. Zettl, W. Mickelson, C. Carraro, and R. Maboudian, "In Situ Localized Growth of Porous Tin Oxide Films on Low Power Microheater Platform for Low Temperature CO Detection," *ACS Sens.*, vol. 1, pp. 339-343, 2016.
- [13] T. Wagner, S. Haffer, C. Weinberger, D. Klaus, and M. Tiemann, "Mesoporous materials as gas sensors," *Chem. Soc. Rev.*, vol. 42, pp. 4036-4053, 2013.
- [14] J. Hodgkinson, and R. P. Tatam, "Optical gas sensing: a review," *Meas. Sci. Technol.*, vol. 24, p. 012004, 2013.
- [15] R. Rubio, J. Santander, L. Fonseca, N. Sabaté, I. Gràcia, C. Cané, S. Udina, and S. Marco, "Non-selective NDIR array for gas detection," *Sens. Actuators B*, vol. 127, pp. 69-73, 2007.
- [16] A. Paliwal, A. Sharma, M. Tomar, and V. Gupta, "Room temperature detection of NO₂ gas using optical sensor based on surface plasmon resonance technique,"

Sens. Actuators B, vol. 216, pp. 497-503, 2015.

[17] L. Ma, L. Wang, R. Chen, K. Chang, S. Wang, X. Hu, X. Sun, Z. Lu, H. Sun, Q. Guo, M. Jiang, and J. Hu, "A Low Cost Compact Measurement System Constructed Using a Smart Electrochemical Sensor for the Real-Time Discrimination of Fruit Ripening," *Sensors*, vol. 16, p. 501, 2016.

[18] M. J. Tierney, and H. -O. L. Kim, "Electrochemical Gas Sensor with Extremely Fast Response Times," *Anal. Chem.*, vol. 65, pp. 3435-3440, 1993.

[19] H. K. Gatty, S. Leijonmarck, M. Antelius, G. Stemme, and N. Roxhed, "An amperometric nitric oxide sensor with fast response and ppb-level concentration detection relevant to asthma monitoring," *Sens. Actuators B*, vol. 209, pp. 639-644, 2015.

[20] F. Liao, C. Chen, and V. Subramanian, "Organic TFTs as gas sensors for electronic nose applications," *Sens. Actuators B*, vol. 107, pp. 849-855, 2005.

[21] H. -W. Zan, C. -H. Li, C. -C. Yeh, M. -Z. Dai, H. -F. Meng, and C. -C. Tsai, "Room-temperature-operated sensitive hybrid gas sensor based on amorphous indium gallium zinc oxide thin-film transistors," *Appl. Phys. Lett.*, vol. 98, p. 253503, 2011.

[22] Q. He, Z. Zeng, Z. Yin, H. Li, S. Wu, X. Huang, and H. Zhang, "Fabrication of flexible MoS₂ thin-film transistor arrays for practical gas-sensing applications," *Small*, vol. 8, pp. 2994-2999, 2012.

[23] I. Lundström, S. Shivaraman, C. Svensson, and L. Lundkvist, "A hydrogen-sensitive MOS field-effect transistor," *Appl. Phys. Lett.*, vol. 26, pp. 55-57, 1975.

[24] M. S. Shivaraman, "Detection of H₂S with Pd-gate MOS field-effect transistors," *J. Appl. Phys.*, vol. 47, pp. 3592-3593, 1976.

[25] U. Ackelid, M. Armgarth, A. Spetz, and I. Lundström, "Ethanol Sensitivity of

Palladium-Gate Metal-Oxide-Semiconductor Structures,” *IEEE Electron Device Lett.*, vol. 7, pp. 353-355, 1981.

[26] M. Josowicz, and J. Janata, “Suspended Gate Field Effect Transistors Modified with Polypyrrole as Alcohol Sensor,” *Anal. Chem.*, vol. 58, pp. 514-517, 1986.

[27] A. Oprea, E. Simon, M. Fleischer, H. -P. Frerichs, C. Wilbertz, M. Lehmann, and U. Weimar, “Flip-chip suspended gate field effect transistors for ammonia detection,” *Sens. Actuators B*, vol. 111, pp. 582-586, 2005.

[28] Z. Gergintschew, P. Kornetzky, and D. Schipanski, “The capacitively controlled field effect transistor (CCFET) as a new low power gas sensor,” *Sens. Actuators B*, vol. 36, pp. 285-289, 1996.

[29] A. Oprea, H. -P. Frerichs, C. Wilbertz, M. Lehmann, and U. Weimar, “Hybrid gas sensor platform based on capacitive coupled field effect transistors: Ammonia and nitrogen dioxide detection,” *Sens. Actuators B*, vol. 127, pp. 161-167, 2007.

[30] C. -H. Kim, I. -T. Cho, J. -M. Shin, K. -B. Choi, J. -K. Lee, and J. -H. Lee, “A New Gas Sensor Based on MOSFET Having a Horizontal Floating-Gate,” *IEEE Electron Device Lett.*, vol. 35, pp. 265-267, 2014.

[31] Y. Hong, S. Hong, D. Jang, Y. Jeong, M. Wu, G. Jung, J. -H. Bae, J. S. Kim, K. S. Chang, C. B. Jeong, C. S. Hwang, B. -G. Park, and J. -H. Lee, “A Si FET-type Gas Sensor with Pulse-driven Localized Micro-heater for Low Power Consumption,” *Proceedings of 2018 IEEE International Electron Devices Meeting (IEDM)*, San Francisco, CA, 1-5 December 2018.

[32] J. Shin, Y. Hong, M. Wu, Y. Jang, J. S. Kim, B. -G. Park, C. S. Hwang, and J. -H. Lee, “Highly Improved Response and Recovery Characteristics of Si FET-type Gas Sensor Using Pre-bias,” *Proceedings of 2016 IEEE International Electron Devices Meeting (IEDM)*, San Francisco, CA, 3-7 December 2016.

[33] B. Sharma, and J. -S. Kim, “MEMS based highly sensitive dual FET gas sensor

using graphene decorated Pd-Ag alloy nanoparticles for H₂ detection,” *Sci. Rep.*, vol. 8, p. 5902, 2018.

[34] X. Liu, S. Cheng, H. Liu, S. Hu, D. Zhang, and H. Ning, “A Survey on Gas Sensing Technology,” *Sensors*, vol. 12, pp. 9635-9665, 2012.

[35] T. Hübert, L. Boon-Brett, G. Black, and U. Banach, “Hydrogen sensors – A review,” *Sens. Actuators B*, vol. 157, pp. 329-352, 2011.

[36] M. Grassi, P. Malcovati, and A. Baschiroto, “A 141-dB Dynamic Range CMOS Gas-Sensor Interface Circuit Without Calibration With 16-bit Digital Output Word,” *IEEE J. Solid-State Circuits*, vol. 42, pp. 1543-1554, 2007.

[37] M. Y. Afridi, J. S. Suehle, M. E. Zaghloul, D. W. Berning, A. R. Hefner, R. E. Cavicchi, S. Semancik, C. B. Montgomery, and C. J. Taylor, “A Monolithic CMOS Microhotplate-Based Gas Sensor System,” *IEEE Sens. J.*, vol. 2, pp. 644-655, 2002.

[38] A. Oprea, N. Bârsan, and U. Weimar, “Work function changes in gas sensitive materials: Fundamentals and applications,” *Sens. Actuators B*, vol. 142, pp. 470-493, 2009.

[39] M. Burgmair, H. -P. Frerichs, M. Zimmer, M. Lehmann, and I. Eisele, “Field effect transducers for work function gas measurements: device improvements and comparison of performance,” *Sens. Actuators B*, vol. 95, pp. 183-188, 2003.

[40] Z. S. Hosseini, A. Irajizad, and A. Mortezaali, “Room temperature H₂S gas sensor based on rather aligned ZnO nanorods with flower-like structures,” *Sens. Actuators B*, vol. 207, pp. 865-871, 2015.

[41] N. Du, H. Zhang, B. Chen, X. Ma, Z. Liu, J. Wu, and D. Yang, “Porous Indium Oxide Nanotubes: Layer-by-Layer Assembly on Carbon-Nanotube Templates and Application for Room-Temperature NH₃ Gas Sensors,” *Adv. Mater.*, vol. 19, pp. 1641-1645, 2007.

- [42] A. Kaniyoor, R. I. Jafri, T. Arockiadoss, and S. Ramaprabhu, "Nanostructured Pt decorated graphene and multi walled carbon nanotube based room temperature hydrogen gas sensor," *Nanoscale*, vol. 1, pp. 382-386, 2009.
- [43] N. S. Ramgir, I. S. Mulla, and K. P. Vijayamohanan, "A room temperature nitric oxide sensor actualized from Ru-doped SnO₂ nanowires," *Sens. Actuators B*, vol. 107, pp. 708-715, 2005.
- [44] Y. Hong, C. -H. Kim, J. Shin, K. Y. Kim, J. S. Kim, C. S. Hwang, and J. -H. Lee, "Highly selective ZnO gas sensor based on MOSFET having a horizontal floating-gate," *Sens. Actuators B*, vol. 232, pp. 653-659, 2016.
- [45] K. Anand, O. Singh, M. P. Singh, J. Kaur, and R. C. Singh, "Hydrogen sensor based on graphene/ZnO nanocomposite," *Sens. Actuators B*, vol. 195, pp. 409-415, 2014.
- [46] S.F. Bamsaoud, S. B. Rane, R. N. Karekar, and R. C. Aiyer, "Nano particulate SnO₂ based resistive films as a hydrogen and acetone vapour sensor," *Sens. Actuators B*, vol. 153, pp. 382-391, 2011.
- [47] N. Barsan, D. Koziej, and U. Weimar, "Metal oxide-based gas sensor research: How to?," *Sens. Actuators B*, vol. 121, pp. 18-35, 2007.
- [48] W. A. Kohler, "Structural Properties of Vapor Deposited Silicon Nitride," *Metall. Mater. Trans. B*, vol. 1, pp. 735-740, 1970.
- [49] K. K. O, N. Park, and D. -J. Yang, "1/f Noise of NMOS and PMOS Transistors and their Implications to Design of Voltage Controlled Oscillators," *2002 IEEE Radio Frequency Integrated Circuits (RFIC) Symposium*, Seattle, WA, USA, 3-4 June 2002.
- [50] J. M. E. Harper, J. J. Cuomo, P. A. Leary, G. M. Summa, H. R. Kaufman, and F. J. Bresnock, "Low Energy Ion Beam Etching," *J. Electrochem. Soc.*, vol. 128, pp. 1077-1083, 1981.

- [51] K. P. Larsen, D. H. Petersen, and O. Hansen, "Study of the Roughness in a Photoresist Masked, Isotropic, SF₆-Based ICP Silicon Etch," *J. Electrochem. Soc.*, vol. 153, pp. G1051-G1058, 2006.
- [52] J. Iqbal, A. Jilani, P. M. Z. Hassan, S. Rafique, R. Jafer, and A. A. Alghamdi, "ALD grown nanostructured ZnO thin films: Effect of substrate temperature on thickness and energy band gap," *J. King Saud Univ. Sci.*, vol. 28, pp. 347-354, 2016.
- [53] B. Ghosh, S. C. Ray, M. Pontsho, S. Sarma, D. K. Mishra, Y. F. Wang, W. F. Pong, and A. M. Strydom, "Defect induced room temperature ferromagnetism in single crystal, poly-crystal, and nanorod ZnO: A comparative study," *J. Appl. Phys.*, vol. 123, p. 161507, 2018.
- [54] S. K. Kim, C. S. Hwang, S. -H. K. Park, and S. J. Yun, "Comparison between ZnO films grown by atomic layer deposition using H₂O or O₃ as oxidant," *Thin Solid Films*, vol. 478, pp. 103-108, 2005.
- [55] Y. Taur, and T. H. Ning, *Fundamentals of Modern VLSI Devices*, Cambridge University Press, New York, NY, USA, 2013.
- [56] Product brochure. Keysight Technologies B1530A (Waveform Generator/Fast Measurement Unit) User's Guide, Edition 7, Keysight Technologies, Inc., Santa Rosa, CA, USA. Available: <http://literature.cdn.keysight.com/litweb/pdf/B1530-90000.pdf>
- [57] G. K. Reeves, and H. B. Harrison, "Obtaining the Specific Contact Resistance from Transmission Line Model Measurements," *IEEE Electron Device Lett.*, vol. 3, pp. 111-113, 1982.
- [58] E. Herth, E. Algré, B. Legrand, and L. Buchaillet, "Optimization of ohmic contact and adhesion on polysilicon in MEMS–NEMS wet etching process," *Microelectron. Eng.*, vol. 88, pp. 724-728, 2011.
- [59] R. A. Butera, and D. H. Waldeck, "The Dependence of Resistance on

Temperature for Metals, Semiconductors, and Superconductors,” *J. Chem. Educ.*, vol. 74, pp. 1090-1094, 1997.

[60] Z. H. Wu, P. T. Lai, and J. K. O. Sin, “A new high-temperature thermal sensor based on large-grain polysilicon on insulator,” *Sens. Actuators A*, vol. 130-131, pp. 129-134, 2006.

[61] Z. Wu, C. Li, J. Hartings, S. Ghosh, R. Narayan, and C. Ahn, “Polysilicon-based flexible temperature sensor for brain monitoring with high spatial resolution,” *J. Micromech. Microeng.*, vol. 27, p. 025001, 2017.

[62] P. Umadevi, and C. L. Nagendra, “Preparation and characterisation of transition metal oxide micro-thermistors and their application to immersed thermistor bolometer infrared detectors,” *Sens. Actuators A*, vol. 96, pp. 114-124, 2002.

[63] C. Yan, J. Wang, and P. S. Lee, “Stretchable Graphene Thermistor with Tunable Thermal Index,” *ACS Nano*, vol. 9, pp. 2130-2137, 2015.

[64] Y. T. Shah, *Thermal Energy: Sources, Recovery, and Applications*, CRC Press, Taylor & Francis Group, FL, USA, 2018.

[65] S. O. Kasap, *Principles of Electronic Materials and Devices*, McGraw-Hill, New York, NY, USA, 2006.

[66] H. Zhao, J. H. Montgomery, N. S. J. Mitchell, and H. S. Gamble, “Buried polysilicon hot-wire anemometer with integrated bulk micromachined channel,” *J. Microlithogr. Microfabr. Microsyst.*, vol. 3, pp. 493-500, 2004.

[67] J. Supadech, E. Ratanaudomphisut, C. Hruanun, and A. Poyai, “Characteristics of silicon thin film thermistors,” *Proceedings of 2008 5th International Conference on Electrical Engineering/Electronics, Computer, Telecommunications and Information Technology (ECTI-CON)*, Thailand, 14-17 May 2008.

- [68] A. Spessot, M. Molteni, D. Ventrice, and P. Fantini, "A Physics-Based Compact Model for Polysilicon Resistors," *IEEE Electron Device Lett.*, vol. 31, pp. 1251-1253, 2010.
- [69] J. Xie, C. Lee, M. -F. Wang, Y. Liu, and H. Feng, "Characterization of heavily doped polysilicon films for CMOS-MEMS thermoelectric power generators," *J. Micromech. Microeng.*, vol. 19, p. 125029, 2009.
- [70] M. S. Raman, T. Kifle, E. Bhattacharya, and K. N. Bhat, "Physical Model for the Resistivity and Temperature Coefficient of Resistivity in Heavily Doped Polysilicon," *IEEE Trans. Electron Devices*, vol. 53, pp. 1885-1892, 2006.
- [71] E. Vereshchagina, R. A. M. Wolters, and J. G. E. Gardeniers, "Measurement of reaction heats using a polysilicon-based microcalorimetric sensor," *Sens. Actuators A*, vol. 169, pp. 308-316, 2011.
- [72] M. Boutchich, K. Ziouche, P. Godts, and D. Leclercq, "Characterization of Phosphorus and Boron Heavily Doped LPCVD Polysilicon Films in the Temperature Range 293-373 K," *IEEE Electron Device Lett.*, vol. 23, pp. 139-141, 2002.
- [73] K. Iniewski, *Nano-Semiconductors: Devices and Technology*, CRC Press, Taylor & Francis Group, FL, USA, 2012.
- [74] A. A. Geisberger, N. Sarkar, M. Ellis, and G. D. Skidmore, "Electrothermal Properties and Modeling of Polysilicon Microthermal Actuators," *J. Microelectromech. Syst.*, vol. 12, pp. 513-523, 2003.
- [75] K. S. Chang, S. C. Yang, J. -Y. Kim, M. H. Kook, S. Y. Ryu, H. Y. Choi, and G. H. Kim, "Precise Temperature Mapping of GaN-Based LEDs by Quantitative Infrared Micro-Thermography," *Sensors*, vol. 12, pp. 4648-4660, 2012.
- [76] H. Lee, K. S. Chang, Y. J. Tak, T. S. Jung, J. W. Park, W. -G. Kim, J. Chung, C. B. Jeong, and H. J. Kim, "Low-temperature activation under 150°C for

amorphous IGZO TFTs using voltage bias,” *J. Inf. Disp.*, vol. 18, pp. 131-135, 2017.

[77] K. Roy, S. Mukhopadhyay, and H. Mahmoodi-Meimand, “Leakage Current Mechanisms and Leakage Reduction Techniques in Deep-Submicrometer CMOS Circuits,” *Proc. IEEE*, vol. 91, pp. 305-327, 2003.

[78] S. Majerus, W. Merrill, and S. L. Garverick, “Design and Long-Term Operation of High-Temperature, Bulk-CMOS Integrated Circuits for Instrumentation and Control,” *Proceedings of 2013 IEEE Energytech*, Cleveland, OH, USA, 21-23 May 2013.

[79] J. I. Kim, K. S. Chang, D. U. Kim, I. -T. Cho, C. -Y. Jeong, D. Lee, H. -I. Kwon, S. H. Jin, and J. -H. Lee, “Thermoreflectance microscopy analysis on self-heating effect of short-channel amorphous In-Ga-Zn-O thin film transistors,” *Appl. Phys. Lett.*, vol. 105, p. 043501, 2014.

[80] S. Y. Ryu, D. U. Kim, J. K. Kim, H. Y. Choi, G. H. Kim, and K. S. Chang, “Surface-Temperature Measurement and Submicron Defect Isolation for Microelectronic Devices Using Thermoreflectance Microscopy,” *Int. J. Thermophys.*, vol. 36, pp. 1217-1225, 2015.

[81] J. Shin, “Highly Improved Response and Recovery Characteristics of FET-type Gas Sensor using Pre-Bias,” Ph.D. dissertation, Seoul National University, Republic of Korea, 2018.

[82] J. A. Aranovich, D. Golmayo, A. L. Fahrenbruch, and R. H. Bube, “Photovoltaic properties of ZnO/CdTe heterojunctions prepared by spray pyrolysis,” *J. Appl. Phys.*, vol. 51, pp. 4260-4268, 1980.

[83] E. Comini, G. Faglia, and G. Sberveglieri, *Solid State Gas Sensing*, Springer Science+Business Media, LLC, New York, NY, USA, 2009.

[84] M. Wu, J. Shin, Y. Hong, X. Jin, and J. -H. Lee, “Pulse Biasing Scheme for the Fast Recovery of FET-Type Gas Sensors for Reducing Gases,” *IEEE Electron*

Device Lett., vol. 38, pp. 971-974, 2017.

[85] M. Wu, C. -H. Kim, J. Shin, Y. Hong, X. Jin, and J. -H. Lee, "Effect of a pre-bias on the adsorption and desorption of oxidizing gases in FET-type sensor," *Sens. Actuators B*, vol. 245, pp. 122-128, 2017.

초 록

가스 센서 기술은 인간 삶의 질을 향상시키는 데에 매우 중요한 역할을 한다. 가스 센서는 대기 오염 및 새집증후군의 원인이 되는 여러 유해한 가스들을 감지할 뿐만 아니라, 질병을 진단하기 위한 의학적 용도 혹은 식자재들의 신선도를 확인하는 용도로도 쓰인다. 가스 센서의 종류로는 대표적으로 저항형, 광학, 전기화학 그리고 전계 효과 트랜지스터(FET)형이 있으며, 그 중 저항형 센서에 대한 연구가 가장 많이 수행되고 있다. 저항형 센서는 구조가 단순하고 공정 과정이 간단하다는 장점이 있으나, 동작에 필요한 충분한 전류 레벨을 얻기 위해서 면적이 큰 단점이 있다. 반면, FET형 가스 센서는 CMOS 공정 기술을 접목할 수 있어 매우 작은 크기로 제작이 가능하고, CMOS 집적 회로와 같은 웨이퍼 상에 동일 공정을 사용하여 집적될 수 있다.

본 논문에서는 종래의 MOSFET 공정 방식을 이용하여 수평형 플로팅 게이트를 갖는 실리콘 FET형 가스 센서를 제작하였다. 제작된 가스 센서는 감지부 하단의 마이크로 히터를 특징으로 한다. 가스와 감지 물질 간의 반응에는 각각마다 반응이 최대가 되는 온도가 존재한다. 이 온도를 조절하기 위해, 일반적으로 가스 센서에는 마이크로 히터가 내장된

다. 종래의 저항형 센서는 감지부의 면적이 크므로 이를 가열하기 위해 마이크로 히터의 면적이 크고 전력 소모도 크다. 하지만, 제작된 가스 센서는 감지부 및 마이크로 히터의 면적이 매우 작게 설계되어 전력 소모도 작다. 고농도로 도핑된 폴리실리콘이 마이크로 히터의 재료로 사용되었고, 추가적인 포토마스크 없이 플로팅 게이트와 동시에 형성되었다. 또한, 마이크로 히터에 의해 발생하는 열의 손실을 줄이기 위해 마이크로 히터의 하단에 공기 층을 형성하였다. 공기 층은 감지부 주변에만 존재하며, 열이 센서의 FET에는 영향을 주지 않도록 설계되었다.

본 논문에서는 마이크로 히터 자체의 저항 측정을 통해 마이크로 히터의 온도를 읽을 수 있는 방법을 제시하였다. 가스 감지 물질로는 산화 아연(ZnO)이 사용되었고, 제작된 가스 센서에 펄스 작동 방법을 적용하여 저전력으로 이산화질소(NO_2) 및 황화수소(H_2S) 가스가 감지된다는 것을 검증하였다.

주요어: 가스 센서, 실리콘 FET형 센서 플랫폼, 로컬 마이크로 히터, 펄스 작동, 온도 측정 방법, 저전력.

학번: 2013-20909

List of Publications

Journals

1. **Yoonki Hong**, Chang-Hee Kim, Jongmin Shin, Kyoung Yeon Kim, Jun Shik Kim, Cheol Seong Hwang, and Jong-Ho Lee, "Highly selective ZnO gas sensor based on MOSFET having a horizontal floating-gate," *Sensors and Actuators B: Chemical*, vol. 232, pp. 653-659, 2016.
2. **Yoonki Hong**, Won-Mook Kang, In-Tak Cho, Jongmin Shin, Meile Wu, and Jong-Ho Lee, "Gas-Sensing Characteristics of Exfoliated WSe₂ Field-Effect Transistors," *Journal of Nanoscience and Nanotechnology*, vol. 17, pp. 3151-3154, 2017.
3. Seongbin Hong, Jongmin Shin, **Yoonki Hong**, Meile Wu, Yujeong Jeong, Dongkyu Jang, Gyuweon Jung, Jong-Ho Bae, and Jong-Ho Lee, "Humidity-Sensitive Field Effect Transistor with In₂O₃ Nanoparticles as a Sensing Layer," *Journal of Nanoscience and Nanotechnology*, vol. 19, pp. 6656-6662, 2019.
4. Yujeong Jeong, Jongmin Shin, **Yoonki Hong**, Meile Wu, Seongbin Hong, Ki Chang Kwon, Seokhoon Choi, Taehyung Lee, Ho Won Jang, and Jong-Ho Lee, "Gas sensing characteristics of the FET-type gas sensor having inkjet-printed WS₂ sensing layer," *Solid State Electronics*, vol. 153, pp. 27-32, 2019.
5. Meile Wu, Jongmin Shin, **Yoonki Hong**, Dongkyu Jang, Xiaoshi Jin, Hyuck-In Kwon, and Jong-Ho Lee, "An FET-type gas sensor with a sodium ion conducting solid electrolyte for CO₂ detection," *Sensors and Actuators B: Chemical*, vol. 259, pp. 1058-1065, 2018.
6. Jongmin Shin, **Yoonki Hong**, Meile Wu, Jong-Ho Bae, Hyuck-In Kwon, Byung-Gook Park, and Jong-Ho Lee, "An accurate and stable humidity

sensing characteristic of Si FET-type humidity sensor with MoS₂ as a sensing layer by pulse measurement,” *Sensors and Actuators B: Chemical*, vol. 258, pp. 574-579, 2018.

7. Seongbin Hong, Jongmin Shin, **Yoonki Hong**, Meile Wu, Dongkyu Jang, Yujeong Jeong, Gyuweon Jung, Jong-Ho Bae, Ho Won Jang, and Jong-Ho Lee, “Observation of physisorption in a high performance FET-type oxygen gas sensor operating at room temperature,” *Nanoscale*, vol. 10, pp. 18019-18027, 2018.
8. Meile Wu, Chang-Hee Kim, Jongmin Shin, **Yoonki Hong**, Xiaoshi Jin, and Jong-Ho Lee, “Effect of a pre-bias on the adsorption and desorption of oxidizing gases in FET-type sensor,” *Sensors and Actuators B: Chemical*, vol. 245, pp. 122-128, 2017.
9. Meile Wu, Jongmin Shin, **Yoonki Hong**, Xiaoshi Jin, and Jong-Ho Lee, “Pulse Biasing Scheme for the Fast Recovery of FET-Type Gas Sensors for Reducing Gases,” *IEEE Electron Device Letters*, vol. 38, pp. 971-974, 2017.
10. Jongmin Shin, **Yoonki Hong**, Meile Wu, and Jong-Ho Lee, “A Wide Detection Range Mercury Ion Sensor Using Si MOSFET Having Single-Walled Carbon Nanotubes as a Sensing Layer,” *IEEE Electron Device Letters*, vol. 38, pp. 959-962, 2017.
11. In-Tak Cho, Jong In Kim, **Yoonki Hong**, Jeongkyun Roh, Hyeonwoo Shin, Geun Woo Baek, Changhee Lee, Byung Hee Hong, Sung Hun Jin, and Jong-Ho Lee, “Low frequency noise characteristics in multilayer WSe₂ field effect transistor,” *Applied Physics Letters*, vol. 106, p. 023504, 2015.

Conferences

1. **Yoonki Hong**, Seongbin Hong, Dongkyu Jang, Yujeong Jeong, Meile Wu, Gyuweon Jung, Jong-Ho Bae, Jun Shik Kim, Ki Soo Chang, Chan Bae Jeong, Cheol Seong Hwang, Byung-Gook Park, and Jong-Ho Lee, "A Si FET-type Gas Sensor with Pulse-driven Localized Micro-heater for Low Power Consumption," *Proceedings of 2018 IEEE International Electron Devices Meeting (IEDM)*, Dec. 2018.
2. **Yoonki Hong**, Yujeong Jeong, Meile Wu, Seongbin Hong, Gyuweon Jung, Dongkyu Jang, and Jong-Ho Lee, "Sensing Characteristics of Si FET-type Humidity Sensor Having a WO₃ Sensing Layer by Using Pulse Scheme," *2019 International Conference on Electronics, Information and Communication (ICEIC 2019)*, Jan. 2019.
3. Meile Wu, Jongmin Shin, **Yoonki Hong**, Dongkyu Jang, Xiaoshi Jin, and Jong-Ho Lee, "Inkjet-Printed PEI FET-Type Humidity Sensor Having a Horizontal Floating-Gate," *The 17th International Meeting on Chemical Sensors (IMCS 2018)*, Jul. 2018.
4. Seongbin Hong, Jongmin Shin, **Yoonki Hong**, Meile Wu, Yujeong Jeong, Jong-Ho Bae, and Jong-Ho Lee, "A Novel FET-type Hydrogen Gas Sensor with Pd-decorated Single-Walled Carbon Nanotubes by Electroplating Method," *The 17th International Meeting on Chemical Sensors (IMCS 2018)*, Jul. 2018.
5. Yujeong Jeong, Jongmin Shin, **Yoonki Hong**, Meile Wu, Seongbin Hong, Dongkyu Jang, Ki Chang Kwon, Seokhoon Choi, Ho Won Jang, and Jong-Ho Lee, "Suppression of Drift in FET-type Gas Sensor Having WS₂ Nanoparticles Using Pulse Measurement," *The 17th International Meeting on Chemical Sensors (IMCS 2018)*, Jul. 2018.
6. Meile Wu, **Yoonki Hong**, Dongkyu Jang, Xiaoshi Jin, and Jong-Ho Lee, "An FET-Type Gas Sensor for CO₂ Detection at Room Temperature Using

- PEI-Coated SWNT,” *2018 Asia-Pacific Workshop on Fundamentals and Applications of Advanced Semiconductor Devices (AWAD 2018)*, Jul. 2018.
7. Dongkyu Jang, **Yoonki Hong**, and Jong-Ho Lee, “A Novel Barometric Pressure Sensor Based on Piezoresistive Effect of Polycrystalline Silicon,” *2018 Asia-Pacific Workshop on Fundamentals and Applications of Advanced Semiconductor Devices (AWAD 2018)*, Jul. 2018.
 8. Jongmin Shin, **Yoonki Hong**, Meile Wu, Younjin Jang, Jun Shik Kim, Byung-Gook Park, Cheol Seong Hwang, and Jong-Ho Lee, “Highly Improved Response and Recovery Characteristics of Si FET-type Gas Sensor Using Pre-bias,” *Proceedings of 2016 IEEE International Electron Devices Meeting (IEDM)*, Dec. 2016.
 9. Meile Wu, Jongmin Shin, **Yoonki Hong**, Xiaoshi Jin, and Jong-Ho Lee, “Effect of APTES Layer on I-V Characteristics of MOSFET-type Gas Sensor Having Solid Electrolyte Sensing Material,” *Nano Korea 2016*, Jul. 2016.
 10. **Yoonki Hong**, Jongmin Shin, Meile Wu, Soo Ho Choi, Yunsik Choi, Seungil Moon, Woochul Yang, and Jong-Ho Lee, “MOSFET-based humidity sensor with inkjet-printed polymer as a sensing layer,” *The 16th International Meeting on Chemical Sensors (IMCS 2016)*, Jul. 2016.
 11. Jong-Ho Lee, **Yoonki Hong**, Meile Wu, and Jongmin Shin, “High Performance Gas Sensors Based on Si MOSFETs,” *The 16th International Meeting on Chemical Sensors (IMCS 2016)*, Jul. 2016.
 12. Jongmin Shin, **Yoonki Hong**, Meile Wu, and Jong-Ho Lee, “Sensing characteristic of lead ion using Si pMOSFET sensor under the different control-gate biases,” *The 16th International Meeting on Chemical Sensors (IMCS 2016)*, Jul. 2016.
 13. Chang-Hee Kim, Chul-Heung Kim, **Yoonki Hong**, Jongmin Shin, Kyu-Bong Choi, In-Tak Cho, Chul-Ho Won, Do-Kywn Kim, Jung-Hee Lee, and

Jong-Ho Lee, “AlGaN/GaN MISFET Gas Sensor Having a Horizontal Floating Gate,” *2015 International Conference on Electronics, Information and Communication (ICEIC 2015)*, Jan. 2015.

14. **Yoonki Hong**, Chang-Hee Kim, Seon-Jin Choi, Il-Doo Kim, and Jong-Ho Lee, “TIN DIOXIDE GAS SENSOR PREPARED BY INKJET PRINTING METHOD,” *The 7th Asia-Pacific Conference of Transducers and Micro-Nano Technology (APCOT 2014)*, Jun. 2014.
15. **Yoonki Hong**, Chang-Hee Kim, Byung Hyo Kim, and Jong-Ho Lee, “Iron Oxide (Fe_3O_4) Gas Sensor Prepared by Inkjet Printing Method,” *The Korean Sensors Society Conference*, Nov. 2013.

Patents

1. Jong-Ho Lee, and **Yoonki Hong**, “FET-TYPE SENSOR ARRAY”
 - Korean Patent KR 10-1954250, Feb. 2019.
2. Jong-Ho Lee, and **Yoonki Hong**, “SENSOR PLATFORM”
 - US Patent filed 15/612,440, Jun. 2017.